#### ORIGINAL RESEARCH ARTICLE



# Coating Characteristics of Plasma-Sprayed Ceramic Thermal Barrier Coatings on Internal Diameter (ID) Surfaces

Maheshwar Rao Bagathi<sup>1</sup> · Robert Vaßen<sup>1,3</sup> · Olivier Guillon<sup>1,2</sup> · Georg Mauer<sup>1,4</sup>

Submitted: 19 February 2025/in revised form: 14 July 2025/Accepted: 14 July 2025/Published online: 6 August 2025 © The Author(s) 2025

**Abstract** Thermal barrier coatings (TBCs) are essential for insulating and protecting components in high-temperature environments, with applications traditionally focused on external surfaces. However, the development of TBCs for internal diameters (ID), particularly for small bores below 200 mm, poses significant challenges due to the limited understanding of coating formation mechanisms in confined geometries and the constraints of process conditions. Therefore, this study aims to elucidate the characteristics of plasma-sprayed ceramic TBCs on ID surfaces, with the goal of establishing a relationship between process parameters, microstructure, and coating properties for 8 wt.% yttria-stabilized zirconia (8YSZ) topcoats applied via atmospheric plasma spraying (APS) using the SM-F100 CONNEX ID torch. The key APS parameters, namely the hydrogen flow rate, current, and spray distance, were investigated using a design of experiments (DOE) methodology to systematically study both the individual and interactive effects of these parameters on coating

systems such as porosity and deposition efficiency, which are critical features of TBC performance. Since ID coatings are constrained by limited space for spray distance and torch placement inside the tubular component, the selection of the appropriate feedstock becomes challenging. Therefore, feedstocks with different morphologies and sizes were investigated and evaluated based on the resulting porosity and deposition efficiency. An agglomerated and sintered 8YSZ feedstock showed the most promising results. In addition, this study also examined the impact of substrate geometry (flat versus curved surfaces) on coating properties and process control. The results contribute to the broader scientific understanding of plasma spray technology for internal diameter (ID) surfaces.

**Keywords** atmospheric plasma spraying (APS) · design of experiments (DOE) · high-temperature applications · internal diameter (ID) plasma spray · thermal barrier coating (TBCs) · yttria-stabilized zirconia (YSZ)

Maheshwar Rao Bagathi m.bagathi@fz-juelich.de

Georg Mauer g.mauer@fz-juelich.de

- Forschungszentrum Jülich GmbH, Institute of Energy Materials and Devices, IMD-2: Materials Synthesis and Processing, 52425 Jülich, Germany
- Jülich Aachen Research Alliance, JARA-Energy, 52425 Jülich, Germany
- Ruhr University Bochum, Department of Mechanical Engineering, Institute for Materials, 44801 Bochum, Germany
- Technical University of Dortmund, Department of Mechanical Engineering, 44227 Dortmund, Germany

#### Introduction

Internal diameter (ID) thermal barrier coatings (TBCs) are protective coatings applied to insulate components exposed to high temperatures and thermal cycling, particularly on inner surfaces of tubes, pipes, and other hollow structures. These coatings act as a thermal barrier, preventing heat transfer from the external environment to the underlying metal. TBCs are commonly used in aero and land-based turbine engines, as well as in blades and burners (Ref 1), where they have significantly contributed to increasing operational efficiency (Ref 2, 3). However, except for burner liners, TBCs are typically applied to the external surfaces of turbine engine components to provide thermal



insulation. Therefore, it is still challenging to coat some hot gas section components, such as pipe bends, which are susceptible to hot corrosion.

TBC systems are composed of three main layers. The ceramic topcoat, typically applied through atmospheric plasma spraying of yttria-stabilized zirconia (YSZ) with 7–8 wt.% Y<sub>2</sub>O<sub>3</sub>-stabilized ZrO<sub>2</sub>, is the most widely used material due to its stability under high temperatures (Ref 4). YSZ also possesses one of the lowest thermal conductivities among ceramics at elevated temperatures, with a value of 2.3 W/m K at 1000 °C for a fully dense material (Ref 5). Beneath the topcoat, the metallic bond coat often composed of MCrAlY alloys (where M can be nickel, cobalt, or both) which provides adhesion and oxidation protection. The third layer, known as the thermally grown oxide (TGO), is a thin oxide layer that forms on the bond coat due to exposure to high temperatures in operation, providing additional oxidation protection.

One of the major challenges in developing ID TBCs has been attributed to the scalability and process integration, primarily due to the lack of appropriate internal diameter high-velocity oxygen fuel (ID-HVOF) spray torches (Ref 6, 7). Traditionally, MCrAlY has been deposited using the HVOF process, which is known to produce high-quality bond coats with low porosity (Ref 8). However, the use of HVOF torch has been limited to external surfaces, as they were not suitable for internal surfaces such as transition ducts and pipes because of the short spray distances and high combustion power, which can result in overheating the substrate and can be detrimental to the torch hardware. The recent development of novel internal diameter HVOF burner technology has now made it possible to apply ID TBCs in various industrial applications, enabling the coating of cylindrical engineering components that were previously not feasible to develop with conventional techniques (Ref 6).

Internal diameter thermal barrier coatings have gained significant attention as a cost-effective engineering solution in the field of advanced ultra-supercritical (AUSC) steam power plants, as they allow the replacement of expensive austenitic stainless steels and Ni-based alloys with conventional steel alloys while improving the performance of transfer pipes (Ref 9), which are applied to the inner surface of the transfer pipes and are designed to withstand the high temperatures (above 700 °C) (Ref 10, 11) found in AUSC power plants. By reducing heat loss through the pipes, ID TBC coatings can help to increase the overall thermal efficiency of the power plant. Consequently, resulting in significant cost savings while also mitigating concerns related to the climate crisis (Ref 9, 12).

Besides, energy and aerospace industries ID TBCs made from yttria-stabilized zirconia (8YSZ) have also shown promise in the automotive industry. Studies by Ekstrom et al. (Ref 13) indicate that such coatings can improve the heat management of the exhaust gases in addition to enhancing the fatigue life of exhaust systems, which is crucial as engines face increasing performance demands and stricter emission standards. Furthermore, research has explored the use of TBCs on cylinder liners to boost fuel efficiency; however, the results have been mixed, while some experiments showed improvements in fuel efficiency, other studies did not observe significant benefits, or the improvements were inconsistent (Ref 14–20). Nevertheless, an optimized small-bore ID coating technique with a selective coating strategy above the top dead center on the cylinder liners of heavy-duty diesel vehicles has been proposed as a potential solution to improve fuel efficiency (Ref 21).

Despite the potential benefits of ID TBCs, several challenges remain, particularly in maintaining coating integrity and adhesion throughout the component's lifespan. Therefore, it is imperative to have understanding of the formation mechanisms of the TBC on the interior surface. The most common techniques used for depositing thermal barrier coatings on components are atmospheric plasma spraying (APS) and electron-beam physical vapor deposition (EB-PVD) (Ref 22, 23). However, the EB-PVD process is not suitable for ID coatings. In the APS process, oxide-ceramic powder is injected into the plasma jet, where the particles are heated and accelerated toward the substrate surface. Upon impact, the molten particles solidify and form splats. The subsequent buildup of such splats results in a coating formation. The porosity is result of unmelted particles and gases trapped during the spray process in the splat accumulation (Ref 24). The deposited coating is sometimes highly defective, containing porosity, and microcracks, which contribute to the low-thermal conductivity of APS TBCs (Ref 4). Typically, the standard APS coatings have porosity of 15–25% (Ref 1).

Preliminary investigations (Ref 7) successfully demonstrated the deposition of an internal diameter (ID) TBC bond coat (CoNiCrAlY) using ID-HVOF, along with the topcoat (8YSZ) applied through ID-APS torches. However, it was reported that the porosity achieved in the topcoat was insufficient for effective TBC application. Feedstock size significantly influences the microstructure of the TBC topcoat and thus its functional properties (Ref 25). Therefore, a critical initial step in the development of ID TBCs is to investigate the optimal processing parameters needed to achieve higher porosity in the topcoat. So, this research addresses key questions to establish a process–microstructure–property relationship for internal diameter TBCs:

1. How do the size and morphology of the ceramic powder feedstock affect the microstructure and properties of the resulting ID TBCs?



- 2. What are the influences of the process parameters on the properties of the ID TBCs?
- 3. How do properties of the TBC compare when applied to flat versus curved substrates?
- 4. What implications does internal coatings have particularly for the spray process?

### **Materials and Methods**

#### Feedstocks

For the initial screening of feedstock in this study, experiments were performed in two sets: Firstly, two distinct particle size fraction 8YSZ powders were selected for investigation. One powder, referred to as the "coarser HOSP powder" (Oerlikon Metco 204NS), had a median particle size ( $d_{50}$ ) of 56 µm and exhibited a spherical morphology as a result of agglomeration and plasma densification (HOSP) methods. The nominal particle size distribution (PSD) for this powder is -125+11 µm. The other powder, referred to as the "finer HOSP powder" (Oerlikon Metco 204F), had a median particle size ( $d_{50}$ ) of 23 µm and also has a spheroidal morphology. The nominal PSD for this powder is -45+15 µm.

Second set of experiments: Two different morphologies of 8YSZ powder were examined. The first powder is the "coarser HOSP powder" as mentioned in the first set of experiments, possessing a HOSP morphology, and the

other powder investigated is HC Starck AMPERIT 827.006 with a median particle size ( $d_{50}$ ) of 72 µm. The latter powder had an agglomerated and sintered structure with a nominal PSD of -125+45 µm. Figure 1(a, b, c) shows the cross section of all used powder feedstock. Some tubular substrates were coated with a cobalt-based MCrAlY bond coat (Praxair Co-210-6; Co-32Ni-21Cr-8Al-0.5Y wt.%) prior to the YSZ topcoat deposition. The bond coat was applied using a specialized internal diameter HVOF torch, "ID-RED" (Thermico Engineering GmbH, Germany).

#### **Substrates**

Initial experiments were aimed to screen various powders and identify those with desired porosity values. Therefore, the powders were deposited on flat stainless-steel substrates without a bond coat. The feedstock displaying the desired porosity levels for TBC application was then deposited on the inner surface of steel tubular substrate to investigate the reproducibility of the coatings using similar process parameters to those used for the flat substrates. For all application relevant trials, including furnace and burner-rig thermal cycling the ceramic topcoat was deposited on tubular specimens only after the inner surface was coated with a CoNiCrAlY bond coat layer (Praxair Co-210-6), which was applied using ID-HVOF.

The flat stainless-steel substrates are of dimensions  $30 \text{ mm} \times 40 \text{ mm} \times 3 \text{ mm}$ , which were grit-blasted with F36 grade alumina sprayed with an air pressure of 2.5 bar

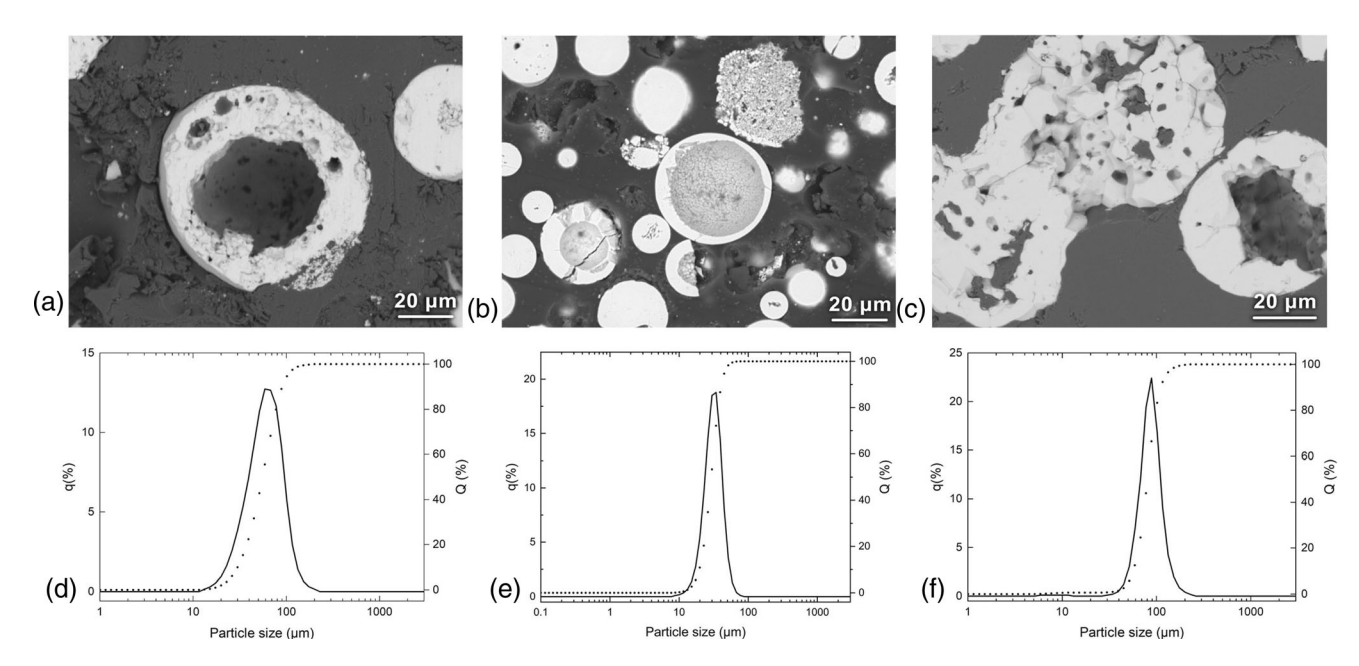


**Fig. 1** Comparison of microstructure and particle size distribution of yttria-stabilized zirconia (8YSZ) feedstock powders. Subfigures (a) and (d) depict the coarser HOSP 8YSZ powder with a median particle size

 $(d_{50})$  of 56  $\mu$ m; (b) and (e) show the finer HOSP 8YSZ powder with a  $(d_{50})$  of 23  $\mu$ m; and (c) and (f) illustrate the agglomerated and sintered (A&S) 8YSZ powder with a  $(d_{50})$  of 72  $\mu$ m



**Table 1** Chemical composition of 1.4878 austenitic stainless-steel tubular substrate

С	Si	Mn	P	S	Cr	Ni	Ti
≤ 0.10	≤ 1.00	≤ 2.00	≤ 0.045	≤ 0.015	17.00-19.00	9.00-12.00	≥ 5(C + N)

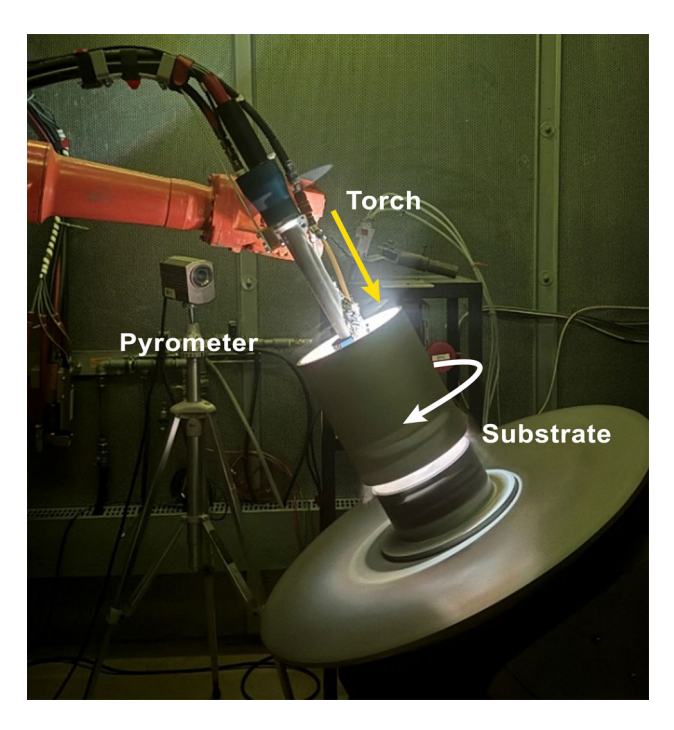


Fig. 2 Atmospheric plasma spraying setup of internal diameter (ID) with F100 CONNEX ID torch

to increase the surface roughness and were then treated in an ultrasonic bath. Prior to the coating, the substrates were preheated without any powder feed by using just the plasma flame.

For the internal diameter (ID) coatings, tubular substrate of 200 mm diameter made of high-temperature austenitic stainless-steel 1.4878 also known as "AISI 321H" or "X10CrNiTi18-10" was used. This type of tubes is used in exhaust systems, furnace parts, and burners, aircraft exhaust manifolds, high-temperature automotive components, industrial ovens, and kilns. Corresponding material properties are listed in Table 1.

# **Thermal Spray Process**

The coatings were generated by an APS Multicoat<sup>TM</sup> facility (Oerlikon Metco, Switzerland) with the use of a SM-F100 CONNEX ID torch with a nozzle diameter of 8 mm mounted on the arm of a six-axis robot, where the tubular substrate rotates on the turning table and the torch moves in the axial direction of the tubular substrate as shown in Fig. 2. The spray process parameters details are given in Table 2.

Table 2 Atmospheric plasma spraying parameters for YSZ based coatings

Current	330-380 (A)
Hydrogen flow	3–5 (slpm)
Argon	30 (slpm)
Carrier gas	2.5 (slpm)
Meander width	2 (mm)
Robot speed	500 (mm/s)
Spray angle	90°
Powder feed rate (HC Starck AMPERIT 827.006)	23 (g/min)
Powder feed rate (Metco 204NS)	24.4 (g/min)
Powder feed rate (Metco 204F)	27.2 (g/min)

slpm: standard liters per minute.

# **Particle Diagnostics**

In this study, the in-flight particle velocities and temperatures were recorded using the optical sensing device DPV-2000 developed by Tecnar, Canada. The system uses infrared pyrometry along with a dual slit mask in order to perform real time in-flight particle temperature, velocity, and diameter. It has a relatively small measurement volume (<1 mm<sup>3</sup>), which allows for the collection of data for individual particles that can be subsequently analyzed statistically. Detailed information on the DPV-2000's operation can be found in literature (Ref 26). Measurements were taken for 5000 particles, and average values of temperature and velocity were calculated. The measurements were performed using an average value of the spray parameters such as hydrogen at 4 slpm and current at 355 A at variable distances ranging from 50 to 120 mm with a 10 mm increment.

# **Porosity**

After the deposition of coatings, the specimens were prepared using standard metallographic preparation techniques for further analysis. The microstructure and porosity were analyzed using a Hitachi SEM TM3000 from Hitachi High Technologies Europe GmbH (Germany). The ImageJ software program was used to evaluate the average porosity by taking at least 5 images per sample at 500× magnification. Regarding the grayscale threshold value used to distinguish between pores and ceramic material, one specific grayscale value was determined from the mean histogram inflection point of a representative subset and



applied to every image in the study under similar brightness and contrast settings. This eliminates run-to-run adjustment and yields reproducible area-fraction values. According to Delesse's stereological principle, the volume fraction can be inferred from the area fraction.

# **Deposition Efficiency**

The deposition efficiency (DE) was calculated as the ratio of the coating weight and the weight of the powder sprayed. The coating weight was determined by the difference in the substrate weight before and after deposition. The weight of the powder sprayed is determined by gravimetrically by a powder feed test. The formula used to calculate the deposition efficiency for the flat substrate is presented in Eq 1, and the Eq 4 represents the deposition efficiency formula for the tubular substrate.

DE (%) = 
$$\left(\frac{S \times V \times 60 \times M_{\text{coating}}}{n \times w \times h \times \dot{m}}\right) 100$$
 (Eq 1)

where "S (mm)" represents the meander width, "V (mm/s)" denotes the speed of the robot, the variable "n" is the number of passes the spray torch makes over the substrate. "w (mm)" and "h (mm)" refer to the width and height of the substrate, respectively,  $M_{\rm coating}$  (g) is weight of coating measured after the deposition of the coating and  $\dot{m}$  (g/min) is the feed rate of the powder sprayed.

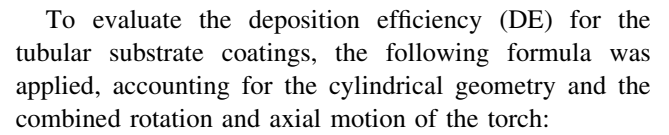
To ensure the same deposition conditions on a tubular substrate with a 200 mm inner diameter, the tubular substrate rotation speed (f) and the axial speed of the robot  $(V_{\rm axial})$  were determined based on the tubular substrate's inner circumference and desired coating overlap. The tubular substrate rotation speed f (revolutions per second) was calculated to match the linear speed of the tubular substrate surface to the flat substrate's torch speed. Given the tubular substrate inner circumference  $C = \pi D = 628.3$  mm, the required rotation speed was:

$$f = \frac{500 \text{mm/s}}{C} = \frac{500}{628 \cdot 3} \approx 0.796 \text{ revolutions per second}$$
(Eq 2)

which corresponds approximately to 48RPM. To maintain the same overlap per revolution, the axial speed of the robot was adjusted so that the torch moved by the meander width "S (mm)" of 2 mm with each full rotation of the tubular substrate. Therefore, the axial speed  $V_{\rm axial}$  was calculated as:

$$V_{\text{axial}} = f \times S = 0.796 \times 2 \approx 1.592 \text{ mm/s}$$
 (Eq 3)

Setting the tubular substrate rotation to 48 RPM and the axial translation to 1.6 mm/s replicated the flat substrate's coating conditions, ensuring uniform thickness and overlap on the internal surface of the tubular substrate.



DE (%) = 
$$\left( \frac{C \times V_{\text{axial}} \times 60 \times M_{\text{coating}}}{n \times \pi D \times L \times \dot{m}} \right) 100$$
 (Eq 4)

where  $C = \pi D$  (mm) is the tubular substrate's inner circumference,  $V_{\rm axial}$  (mm/s) is the axial speed of the torch, n is the number of passes the spray torch makes over the tubular substrate's internal surface, D (mm) is the inner diameter of the tubular substrate, L (mm) is the axial length of the coated area,  $M_{\rm coating}$  (g) weight of coating measured after the deposition of the coating, and  $\dot{m}$  (g/min) is the feed rate of the powder sprayed.

# **Design of Experiments (DOE)**

In this study, a statistical design of experiments (DOE) approach was employed to systematically investigate the individual and interactive effects of variable plasma spray parameters on key coating characteristics. Specifically, porosity, deposition efficiency, and net plasma power—key factors for thermal barrier coatings (TBCs) were evaluated as response variables influenced by these parameters. A full factorial 2<sup>3</sup> design was implemented with eight experimental runs to vary three critical parameters: hydrogen flow rate, current, and spray distance.

Each experimental parameter was defined as a continuous numeric factor: Hydrogen flow rates were set at 3 slpm and 5 slpm, current was controlled at 330A and 380A, and the spray distance was varied between 70 mm and 120 mm. By treating these factors as continuous variables, the design allowed for a comprehensive analysis of their influences on coating characteristics, utilizing a second-order polynomial regression model. This model functionally relates the system response to parameter variations, represented by the equation:

$$\begin{split} Y &= \beta_0 + \beta_1 A + \beta_2 B + \beta_3 C + \beta_{12} A B + \beta_{23} B C + \beta_{13} A C \\ &+ \beta_{11} A^2 + \beta_{22} B^2 + \beta_{33} C^2 \end{split} \tag{Eq 5}$$

where Y represents the response variables of interest, such as porosity or deposition efficiency or net plasma power, and A, B, and C denote spray distance, current, and hydrogen flow, respectively, and  $\beta_0$  through  $\beta_{33}$  are the regression coefficients. The model parameters were derived using Design-Expert v13 software (Stat-Ease Inc.), which calculated these coefficients based on the experimental data to predict system responses effectively. The calculation methods can be found elsewhere (Ref 27). The model was assessed through analysis of variance (ANOVA), enabling



the examination of the statistical significance of each factor and their interactions on the response variables. The coefficients in the coded form of the equation enabled direct comparison of the relative influence of each parameter by normalizing the factor levels to values of +1 or -1, corresponding to their maximum and minimum settings. The actual equation, utilizing the original units of each parameter, provided a direct prediction of response values at specified parameter levels. Table 3 lists the eight test runs used in the design of experiments for the ID-APS TBC trials, showing each run's combination of spray distance, plasma current, and hydrogen flow rate.

To refine the model and eliminate nonsignificant terms, only terms with a probability value (p value) less than 0.1 were considered. The model's quality and reliability were further evaluated through R-squared ( $R^2$ ), adjusted  $R^2$ , and predicted  $R^2$  values, which collectively indicated the model's goodness of fit, accuracy in reflecting experimental data, and capability to predict new data points.

#### **Fracture Surface Analysis**

Fracture surface analysis was conducted to examine the microstructure of the yttria-stabilized zirconia (8YSZ) topcoat coatings. To facilitate this analysis, the 8YSZ coatings were prepared as free-standing layers by detaching them from their substrates. Although several methods for substrate removal are documented in the literature (Ref 28), in this study, an electrochemical method was employed. A concentrated salt solution served as the electrolyte, and a voltage was applied to induce coating detachment. Once separated, the coatings were deliberately fractured to expose the internal surfaces for analysis. The fractured surfaces were then examined using scanning electron microscopy (SEM) to assess their microstructural features.

**Table 3** Experimental runs defined by the 2<sup>3</sup> full factorial DOE-spray parameter combinations

Run	Spray distance (mm)	Current (A)	Hydrogen flow (slpm)
1	120	330	5
2	120	330	3
3	70	330	5
4	70	380	3
5	70	330	3
6	120	380	3
7	120	380	5
8	70	380	5

#### Thermographic Measurements

Thermographic measurements were performed using a PI 640i thermal camera (Optris GmbH, Germany) to characterize the heat distribution across the surface of the tubular substrate during coating deposition. These measurements provide critical insights into the thermal load experienced by the substrate, informing the potential need for an active cooling system to maintain thermal stability throughout the spray process. By capturing heat distribution data, this analysis enables a deeper understanding of the relationship between substrate heating and the layer formation mechanism. The deposition temperature was directly monitored by a pyrometer, while the thermal camera continuously recorded the substrate's surface temperature from the exterior. The resulting thermal data were processed using the Optris PIX Connect software package. To ensure uniform emissivity across the substrate and thereby enhance the accuracy of temperature measurements, the tubular substrate surfaces were pretreated with a layer of black graphite spray, which remained stable throughout the process.

#### **Residual Stress Measurements**

The in situ coating property (ICP) sensor from Reliacoat Technologies LCC (East Setauket, USA) was utilized to monitor the evolution of residual stress during the thermal spray process. This technique measures the curvature of the substrate as the coating is applied, providing insights into the stresses induced by thermal gradients and the thermal expansion mismatch between the substrate and the coating. A laser-based sensor system continuously tracks changes in substrate curvature as coating layers accumulate. The standard sample preparation was followed as described in (Ref 29), using stainless-steel samples with dimensions of 228 mm × 25 mm × 2 mm. Detailed formulations and coating stress evaluation methods used can be found in references (Ref 24, 29).

## **Results and Discussion**

### **Screening of Powders**

In this study, screening of various feedstocks was performed to identify optimal ceramic feedstock for coating internal diameter (ID) surfaces using a specialized ID plasma torch. The investigation focused on powders with identical morphology but varying sizes, as well as powders with differing morphologies, to determine the impact of these variations on coating characteristics. The evaluation involved selecting process parameters within the allowable

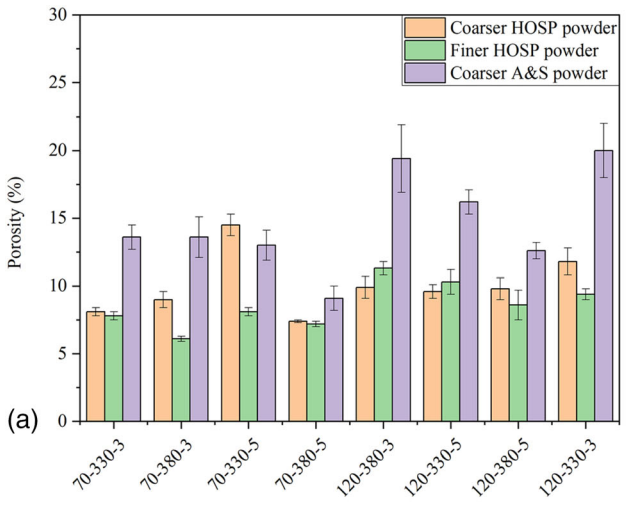


range (hydrogen flow rates (0–6 slpm) and current levels (up to 450A)) for the F100 CONNEX torch. These values represent the operational limits specified by the torch manufacturer.

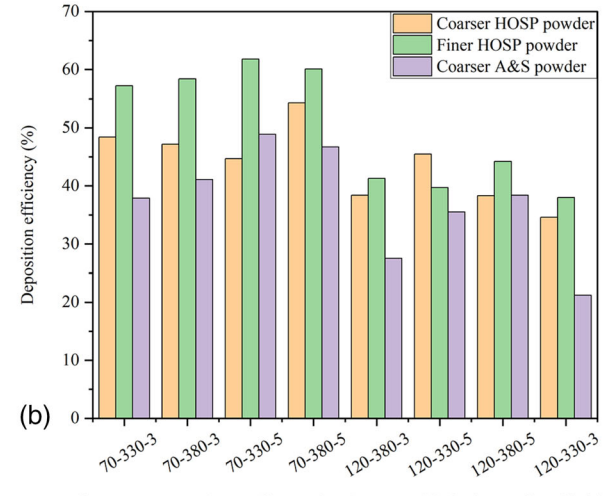
Figure 3 presents a comparison of (a) porosity and (b) deposition efficiency of yttria-stabilized zirconia (8YSZ)-based thermal barrier coatings (TBCs) deposited using an internal diameter atmospheric plasma spray (IDAPS) torch under various spray parameters. For powders with HOSP morphology, the finer HOSP powder consistently produces coatings with lower porosity than the coarser HOSP powder at both 70 mm and 120 mm spray distances. This trend aligns with the observed deposition

efficiency, where coatings made from the finer HOSP powder demonstrate higher deposition efficiency across all spray distances. Interestingly, this observation does not align with existing literature (Ref 30) which generally favors finer feedstock for ID coatings for certain applications.

When comparing coatings deposited with powders of different morphologies but similar coarser particle sizes, the coarser A&S powder results in coatings with higher porosity and lower deposition efficiency compared than the coarser HOSP powder. This disparity indicates the substantial impact of particle morphology on coating deposition in ID-APS processes. The cross-sectional SEM images



Spray parameters (spray distance (mm), current (A), hydrogen flow (l/min))



Spray parameters ( spray distance (mm), current (A), hydrogen flow (l/min))

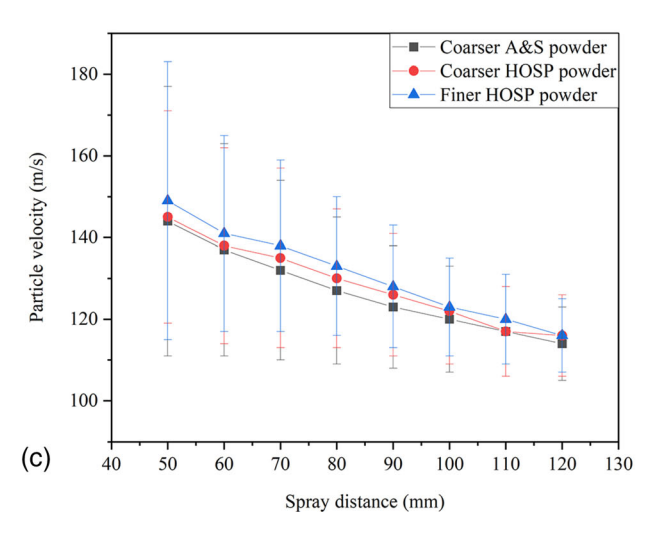
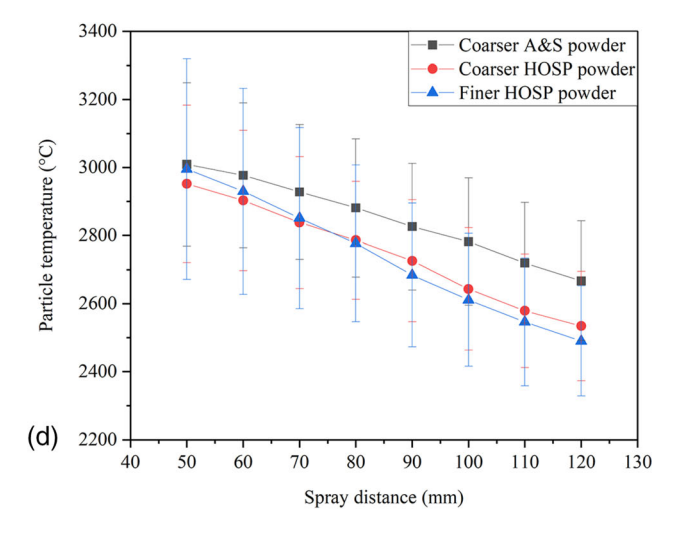


Fig. 3 Comparison of yttria-stabilized zirconia (8YSZ)-based thermal barrier coatings (TBCs) deposited using an internal diameter atmospheric plasma spray (ID-APS) torch with varying feedstock morphologies and particle sizes. (a) illustrates the porosity of coatings, the error bars represent the standard deviation in porosity measurements, while (b) presents the deposition efficiency under



different spray parameters (spray distance, current, and hydrogen flow rate). (c) and (d) show particle diagnostic data for the coatings applied with the F100 CONNEX ID torch sprayed with 355A current and 4 slpm hydrogen flow at varying spray distances, displaying particle velocity (m/s) in (c) and particle temperature (°C) in (d), both measured using the DPV-2000 system



in Fig. 4 further support these observations, where subfigure (a) shows coatings made with the coarse HOSP powder, exhibiting a porosity of  $9 \pm 0.6\%$ , subfigure (b), representing the coating with finer HOSP powder, demonstrates the lowest porosity of 6.1  $\pm$  0.2%, indicating highly dense microstructures with minimal voids. In contrast, subfigure (c), depicting the coating with agglomerated and sintered (A&S) powder, reveals a significantly higher porosity of  $13.6 \pm 1.5\%$ , characterized by larger voids. Across all powder types, coatings sprayed at a 70 mm distance show lower porosity and higher deposition efficiency than those applied at 120 mm. These findings emphasize the combined influence of feedstock morphology and particle size on coating characteristics, as noted in previous studies (Ref 31, 32), and highlight the critical role of spray distance optimization in ID TBC applications.

The interaction between plasma and particles during the spray process is governed by heat transfer and momentum transfer, which influence the extent of particle melting and acceleration prior to deposition. Heating occurs as thermal energy is transferred from the hot plasma gases to the particle, while acceleration is driven by the transfer of momentum from fast-moving ions and gas atoms. The particle's velocity is thus influenced by the drag force  $F_{\rm d}$  which impacts its dwell time ( $t_{\rm dw}$ ) in the plasma. From the

literature (Ref 33) it could be characterized by two more characteristic times. The heat absorption time ( $t_{ha}$ ) that represents the time required for the particle to achieve a uniform internal temperature, and the heat supply time ( $t_{hs}$ ), which is the time needed to raise the particle's temperature to a target mean temperature ( $T_p$ ). These time scales depend on the particle's thermal properties, including thermal conductivity, density, and specific heat capacity. The heat transfer coefficient (h) is determined using the Nusselt number (Nu), a dimensionless parameter that captures the influence of flow conditions on convective heat transfer. For this study, Nu is taken as 2 (Ref 34). Plasma properties, including plasma temperature (estimated at 8000 K), thermal conductivity, and viscosity, are referenced from (Ref 35) for this evaluation.

The finer HOSP powder due to their small size  $(d_{50} = 23 \, \mu\text{m})$  and hollow morphology have the shortest heat absorption time  $(t_{\text{ha}})$  of  $3.15 \times 10^{-5} \, \text{s}$  and a heat supply time  $(t_{\text{hs}})$  of  $3.94 \times 10^{-5} \, \text{s}$ . These values reflect that finer particles with higher surface area-to-volume ratios heat rapidly in the plasma. Although it has low heat transfer  $(q = 0.09 \, \text{W})$ , consistent with its smaller particle size, the high heat transfer coefficient  $(h = 43,478 \, \text{W/m·K})$  of the finer HOSP powder supports efficient internal heat distribution, resulting in temperatures on the surface of the

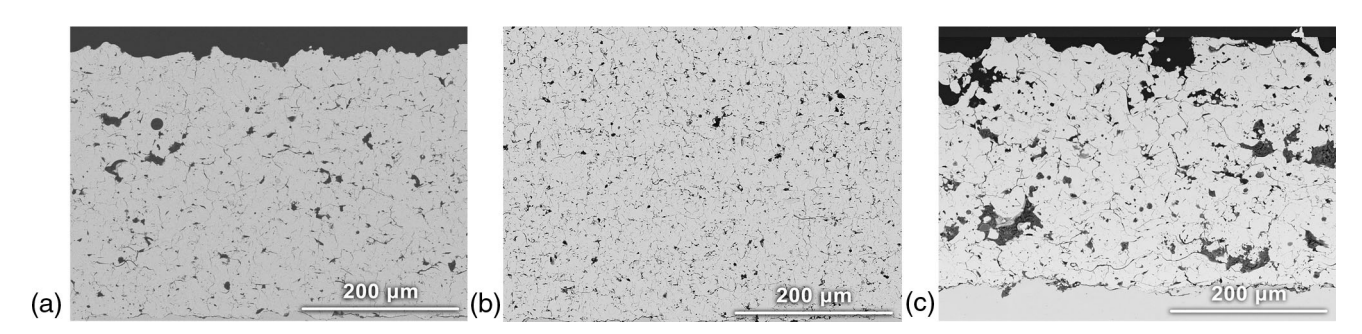


**Fig. 4** Cross-sectional SEM comparison of yttria-stabilized zirconia (8YSZ) coatings produced using different feedstock powders, all deposited at a spray distance of 70 mm, a current of 380 A, and a hydrogen flow of 3 slpm with the F100 CONNEX ID torch.

Subfigures present coatings produced with (a) coarser HOSP 8YSZ, resulting in a porosity of  $9\pm0.6\%$ ; (b) finer HOSP 8YSZ, with a porosity of  $6.1\pm0.2\%$ ; and (c) agglomerated and sintered (A&S) 8YSZ, showing a porosity of  $13.6\pm1.5\%$ 

Table 4 Plasma-particle interaction analysis for different feedstocks of internal diameter (ID) sprayed thermal barrier coatings (TBCs)

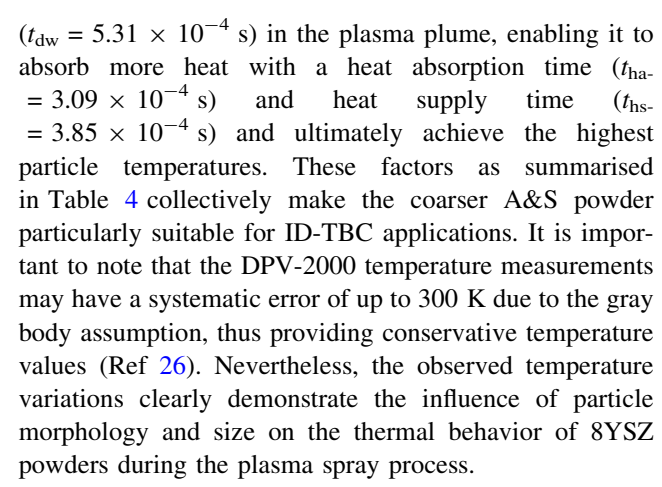
Powder type	Heat absorption time (s)	Heat supply time (s)	Dwell time for 70 mm spray distance (s)	Dwell time for 120 mm spray distance (s)	Heat transfer coefficient (W/m K)	Heat transfer (W)
HOSP powder $(d_{50} = 23 \mu m)$	$3.15 \times 10^{-5}$	$3.94 \times 10^{-5}$	$5.07 \times 10^{-4}$	$1.03 \times 10^{-3}$	43,478	0.09
HOSP powder $(d_{50} = 56 \mu m)$	$1.87 \times 10^{-4}$	$2.33 \times 10^{-4}$	$5.18 \times 10^{-4}$	$1.03 \times 10^{-3}$	17,857	0.22
A&S powder $(d_{50} = 72 \mu \text{m})$	$3.09 \times 10^{-4}$	$3.85 \times 10^{-4}$	$5.31 \times 10^{-4}$	$1.05 \times 10^{-3}$	13,889	0.28



particles of 2956 °C at 70 mm and 2490 °C at 120 mm spray distance. However, this powder experiences the lowest drag force  $(2.08 \times 10^{-6} \text{ N})$ , which enables it to reach the highest velocities among the powders around 138 m/s at 70 mm and 116 m/s at 120 mm spray distance. Due to their higher velocity, the finer HOSP particles have a shorter dwell time ( $t_{\rm dw} = 5.07 \times 10^{-4} \text{ s}$ ) in the plasma plume, which limits their heat absorption. As a result, they reach the substrate in a partially molten or rapidly solidifying state, leading to the formation of a dense, cohesive coating with minimal porosity upon impact.

The coarser HOSP powder exhibits intermediate thermal and momentum transfer characteristics. With a heat absorption time ( $t_{\rm ha}=1.87\times 10^{-4}~\rm s$ ) and heat supply time ( $t_{\rm hs}=2.33\times 10^{-4}~\rm s$ ), this powder achieves sufficient internal temperature within the dwell time ( $t_{\rm dw}=5.18\times 10^{-4}~\rm s$ ). The heat transfer coefficient for this powder is moderate ( $h=17,857~\rm W/m\cdot K$ ), reflecting reduced thermal conductivity compared to the finer HOSP powder, likely due to its larger size and thicker particle structure. The higher heat transfer ( $q=0.22~\rm W$ ) ensures adequate heating, leading to particle temperatures of 2838 °C at 70 mm and 2534 °C at 120 mm. The coarser HOSP powder experiences a moderate drag force (5.43  $\times$  10<sup>-6</sup> N), resulting in particle velocities of 135 m/s at 70 mm and 116 m/s at 120 mm.

In contrast, the coarser agglomerated and sintered (A&S) powder consistently reaches the highest particle temperatures across all spray distances, with values of 2928 °C at 70 mm and 2667 °C at 120 mm spray distance. This high temperature is a result of several key factors. The coarser A&S powder has the highest heat transfer (q = 0.283 (W)). This higher heat transfer indicates that more energy is absorbed by the particle per unit of time, resulting in an increased temperature. The high heat transfer is likely due to the larger mass and denser structure of the A&S powder, which has a larger surface area available to absorb energy from the plasma plume compared to more compact or finer particles. Despite the high heat transfer, the coarser A&S powder has a relatively low heat transfer coefficient ( $h = 13,888 \text{ W/m} \cdot \text{K}$ ), which indicates that the heat distribution within the particle is less efficient than in the other powders. This lower efficiency leads to a temperature gradient within the particle, with the outer regions heating up more quickly and achieving higher surface temperatures. The coarser A&S powder has the largest dimensions and mass, so it experiences the highest drag force (7.48  $\times$  10<sup>-6</sup> N). However, its greater inertia causes it to accelerate more slowly, never reaching the higher velocities of smaller powders. Therefore, the lower velocity (132 m/s at 70 mm spray distance, dropping to 114 m/s at 120 mm) as compared to other powders investigated then increases its dwell time



Effect of process parameters on deposition process and coating properties

Table 5 summarizes the eight experiments of the 2<sup>3</sup> full-factorial design used to quantify how spray distance (mm), current (A), and hydrogen flow (slpm) influence the ID-APS process. Each run produced responses-net plasma power, deposition efficiency (DE), and porosity-which were then subjected to ANOVA to identify the statistically significant main effects and interactions.

#### **Porosity**

The systematic investigation into the effect of process parameters on coating porosity, analyzed through ANOVA, produced a statistically significant linear model with an F value of 19.79 and a p value of 0.0042. This indicates that the model effectively explains a significant portion of the variability in porosity, with spray distance (A) and hydrogen flow (C) emerging as key contributors as listed in Table 6.

Both spray distance and hydrogen flow exhibit significant effects on porosity, with p values of 0.0024 and 0.0419, respectively. The standardized coefficient estimate (measured on a scale of -1 to 1) for spray distance is 0.83, suggesting that each standard unit increase in spray distance results in a 0.83 standard unit increase in porosity. In contrast, the negative standardized coefficient for hydrogen flow (-0.4) implies that increased hydrogen flow decreases porosity. This indicates that spray distance adjustments have a more substantial impact on porosity than similar adjustments in hydrogen flow. With longer spray distance, the particles dwell time increases which allows them to cool down before reaching the substrate, as a result fewer particles remain above the melting temperature. Conversely, higher hydrogen flow enhances the plasma plume's thermal conductivity, enabling more heat transfer to particles, which improves melting and decreases porosity. This effect is observed at 120 mm and 5 slpm, where porosity is lower than at 120 mm and 3 slpm.



DE (%) Run A: Spray distance (mm) B: Current (A) C: Hydrogen (slpm) Net plasma power (kW) Porosity (Vol.%) 120 5 1 330 10 33.7 17 2 120 330 3 8.9 24.3 23.2 3 70 330 5 9.8 46 10.6 70 3 4 380 10 44.5 12.7 5 70 330 3 36.7 14.1 86 3 17.9 6 120 380 9.5 35.4 7 120 5 11 39.7 17.2 380 70 5 47.4 9.5

Table 5 Experimental matrix with the system responses of as-sprayed coatings

380

Table 6 ANOVA and fit statistics for regression model of coating porosity

8

Source	Sum of squares	df	Mean square	F value	p value	
Model	123.94	2	61.97	19.79	0.0042	Significant
A-spray distance	100.82	1	100.82	32.20	0.0024	
C-hydrogen	23.12	1	23.12	7.38	0.0419	
Residual	15.66	5	3.13			
Cor total	139.59	7				
Std. Dev.	1.77	$R^2$	0.8879			
Mean	15.28	Adjusted $R^2$	0.8430			
C.V. %	11.28	Predicted R <sup>2</sup>	0.7129			
		Adeq precision	9.6902			

10.9

The model demonstrates strong reliability, with an  $R^2$  of 0.89 (88.79% of variation explained), an adjusted  $R^2$  of 0.84, and a predicted  $R^2$  of 0.7, all supporting the model's predictive capability. An adequate precision value of 9.9602, well above the recommended threshold of 4, confirms a strong signal-to-noise ratio. The variance inflation factor (VIF) of 1.000 for both spray distance and hydrogen flow indicates no multicollinearity, affirming that each factor independently influences porosity. Figure 5(a) presents the surface response plot generated by the regression Eq 6 in coded factors

$$Y_{\text{porosity}} = 15.27 + 3.55 \text{(spray distance (mm))}$$
  
-1.7(hydrogen flow (slpm)) (Eq 6)

# **Deposition Efficiency**

The fit summary proposed a linear model to calculate and predict the deposition efficiency (DE). Using a hierarchical search, only significant terms were retained, with all terms showing significance at p < 0.05. The model's F value from ANOVA was statistically significant, indicating that the likelihood of this F value arising due to random noise is less than 0.67%. This confirms that the model's effects are real and not due to random fluctuations.

The standardized coefficient estimates of each variable's relative influence on DE reveal that spray distance has the largest negative influence on DE with -0.75, followed by current and hydrogen flow, both of which positively affect DE with 0.47. This is consistent with the F values from the ANOVA as listed in Table 7, which support the significance of these factors.

A higher current generates more power, increasing the plasma's specific enthalpy and temperature, which enhances heat transfer to particles. This, in turn, can lead to higher plasma velocity, depending on gas flow conditions. A higher plasma temperature may also lead to an increase in plasma velocity, which influences particle acceleration and residence time in the hot zone, further affecting melting efficiency. Similarly, higher hydrogen content raises the plasma temperature (Ref 36) and improves thermal conductivity, allowing more energy transfer to the injected particles, promoting melting and increasing DE.

The model fit is supported by a high coefficient of determination  $(R^2)$  of 0.9395, indicating that only 6.05% of the total variation is unexplained by the model. The predicted  $R^2$  of 0.7581 aligns well with the adjusted  $R^2$  of 0.8941, as the difference is less than 0.2, indicating the model's predictive reliability within the design space. The regression Eq (7) presents the surface response plots of DE



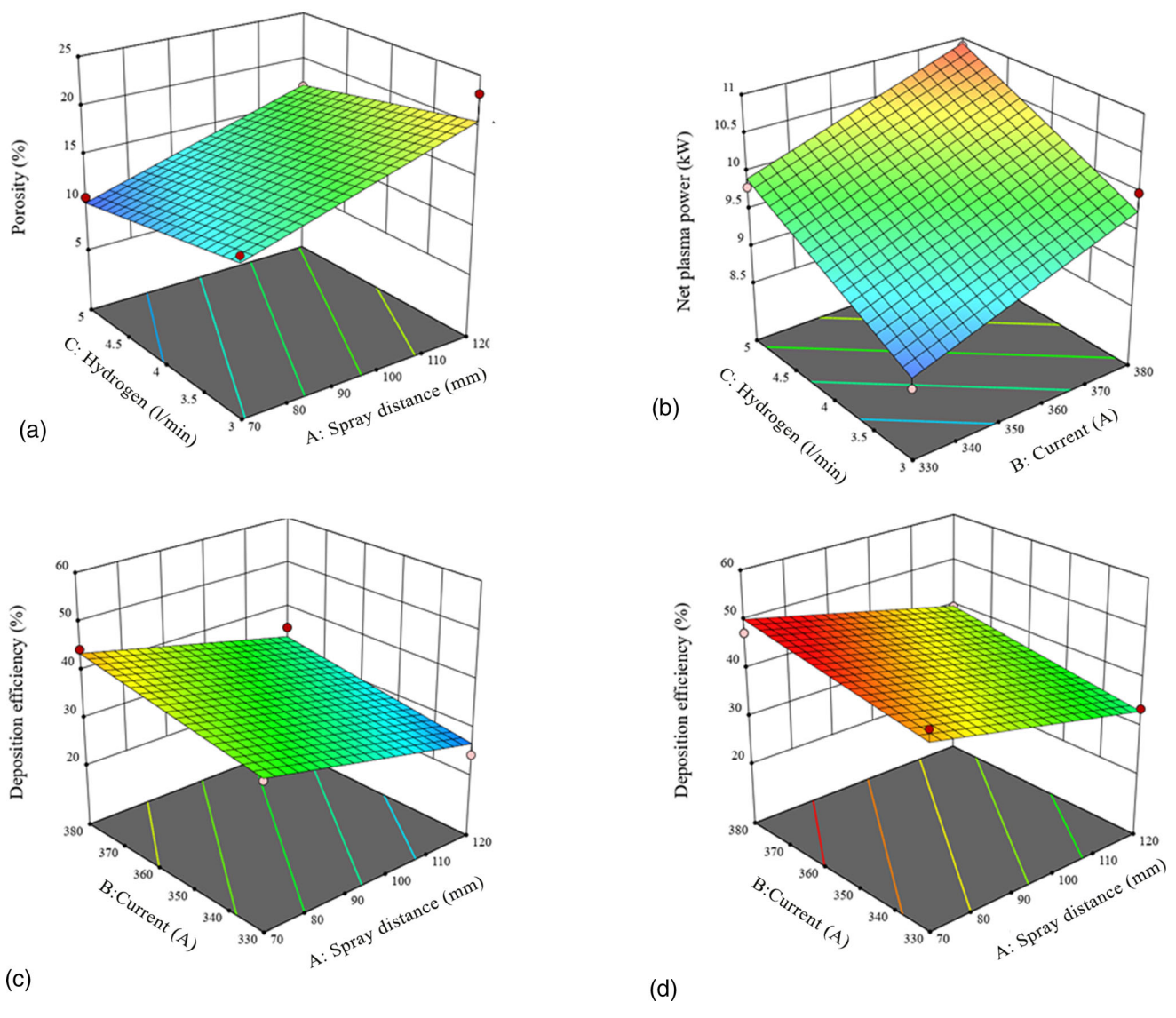


**Fig. 5** Surface plots showing the effects of various spray parameters on the properties of yttria-stabilized zirconia (8YSZ)-based thermal barrier coatings (TBCs). Where (a) displays the porosity (%) as a function of spray distance and hydrogen flow rate, while (b) shows the

net plasma power (kW) relative to current and hydrogen flow. Subfigures (c) and (d) illustrate the deposition efficiency (%) as influenced by spray distance and current, with (c) at a hydrogen flow of 3 slpm and (d) at 5 slpm

**Table 7** ANOVA and fit statistics for deposition efficiency regression model

Source	Sum of squares	df	Mean square	F value	p value	
Model	385.59	3	128.53	20.71	0.0067	Significant
A-spray distance	215.28	1	215.28	34.69	0.0042	
B-current	86.46	1	86.46	13.93	0.0203	
C-hydrogen	83.85	1	83.85	13.51	0.0213	
Residual	24.82	4	6.21			
Cor total	410.42	7				
Std. Dev.	2.49	$R^2$	0.9395			
Mean	38.46	Adjusted $R^2$	0.8941			
C.V. %	6.48	Predicted R <sup>2</sup>	0.7581			
		Adeq precision	13.2978			



with current and spray distance at 3 slpm hydrogen flow in Fig. 5(c) and in (d) at 5 slpm.

$$Y_{\rm DE} = 38.46 - 5.19 (\text{spray distance (mm)}) + 3.29 (\text{current (A)}) + 3.24 (\text{hydrogen flow (slpm)})$$
(Eq 7)

#### **Net Plasma Power**

The systematic analysis of process parameters affecting the net plasma power, evaluated through ANOVA, yielded a statistically linear model with an F value of 61.94 and a p value of 0.0003, confirming that the model effectively captures key variations in net plasma power as listed in Table 8. Current (B) and hydrogen flow (C) were identified as significant contributors.

The impact of current and hydrogen flow rate on net plasma power was statistically significant with p values well below 0.05 reflecting their importance in the model. The standardized coefficient estimate for hydrogen flow is 0.74, indicating that each standard deviation increase in hydrogen flow results in a 0.74 standard deviation increase in net plasma power. Similarly, the current shows a positive standardized coefficient of 0.64, suggesting that increase in currents also lead to higher net plasma power. This indicates that while both factors contribute positively, hydrogen flow has a slightly greater influence. Higher current increases the power input into the plasma torch since power  $P = V \times I$ , leading to a higher energy density within the plasma. With higher current, there is more ionization of the plasma gas (Ar/H<sub>2</sub> mixture), leading to a higher enthalpy of the plasma therefore enhances the temperature and velocity of the plasma plume (Ref 36). Likewise, higher hydrogen flow improves plasma thermal conductivity thus raising the plasma power; at 380 A and 5 slpm hydrogen flow, the model shows the highest plasma power and the gradient in Fig. 5(b) from blue (lower power) to red (higher power) visually confirm that lower setting for either parameter results in decreased plasma power.

**Table 8** ANOVA results and model fit statistics for regression model of net plasma power

Source	Sum of squares	df	Mean square	F value	p value	
Model	4.86	2	2.43	61.94	0.0003	Significant
B-current	2.10	1	2.10	53.54	0.0007	
C-hydrogen	2.76	1	2.76	70.35	0.0004	
Residual	0.1962	5	0.0392			
Cor Total	5.06	7				
Std. Dev.	0.1981	$R^2$	0.9612			
Mean	9.84	Adjusted $R^2$	0.9457			
C.V. %	2.01	Predicted R <sup>2</sup>	0.9007			
		Adeq precision	18.1337			

The model demonstrates strong reliability, with an  $R^2$  of 0.9612 (indicating that 96.12% of the variation in net plasma power is explained by the model), an adjusted  $R^2$  of 0.9457, and a predicted  $R^2$  of 0.9007, all of which support the model's predictive accuracy. Additionally, the adequate precision value of 18.133, well above the threshold of 4, confirms a favorable signal-to-noise ratio. The variance inflation factor (VIF) of 1.000 for both current and hydrogen flow indicates the absence of multicollinearity, verifying that each factor independently influences net plasma power. Figure 5(b) surface plot shows the interaction between current and hydrogen flow on net plasma power shown by the Eq (8)

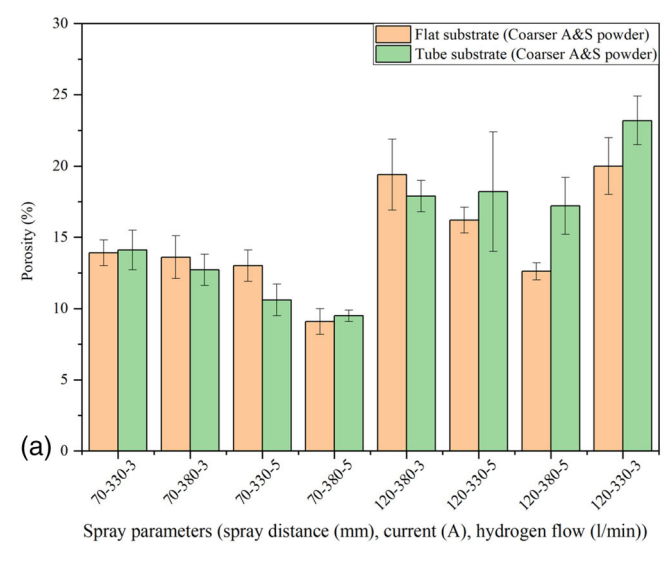
$$Y_{\text{netplasmapower}} = 9.84 + 0.51(\text{current } (A)) + 0.59(\text{hydrogen flow (slpm}))$$
 (Eq 8)

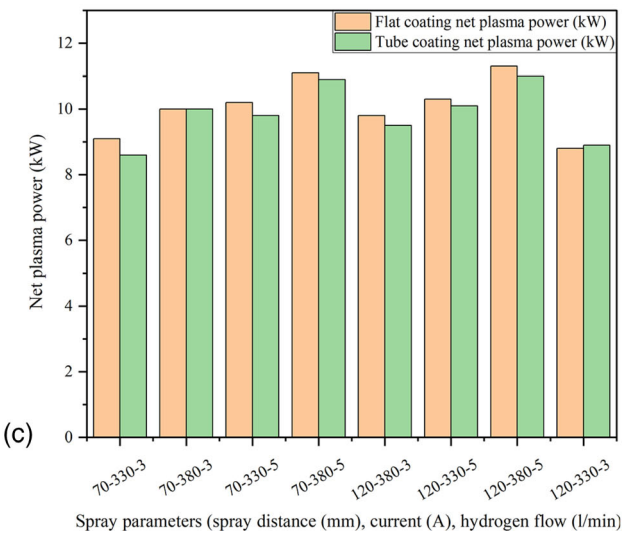
# **Effect of Substrate Curvature on Deposition Process** and Coating Porosity

Following a careful selection of the feedstock, coatings with coarser size agglomerated and sintered feedstock were deposited on the internal diameter (ID) surfaces of tubular substrates to assess the impact of substrate geometry on coating characteristics. From Fig. 6, porosity, deposition efficiency, net plasma power, and deposition temperature of thermal barrier coatings (TBCs) deposited on flat and tubular substrates were analyzed under different spray parameters.

The porosity values for both flat and tubular substrates are comparable, with overlap in error bars across most spray parameter combinations. The results in Fig. 6(a) show that porosity varied significantly with spray distance, current, and hydrogen flow rate. Coatings deposited at a spray distance of 70 mm with higher current (380 A) and hydrogen flow (5 slpm) demonstrated lower porosity on both flat and tubular substrates, while coatings applied at a lower current (330 A) and hydrogen flow (3 slpm) exhibited higher porosity. Similarly, for coatings sprayed at a 120 mm distance (Fig. 6b), the low-porosity

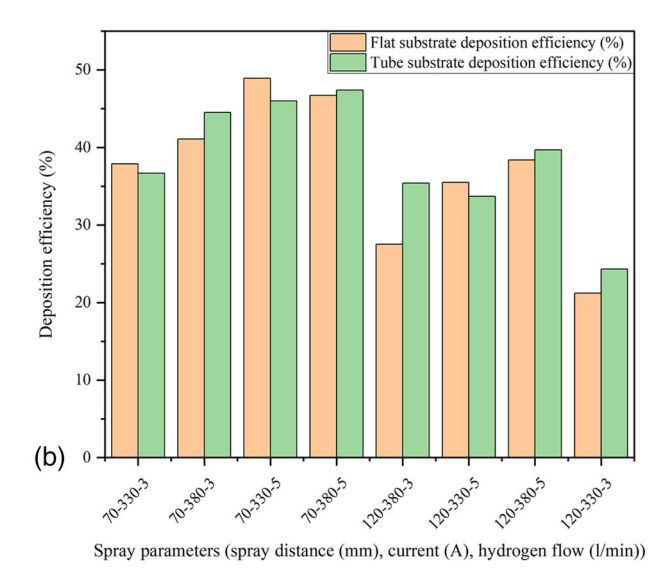


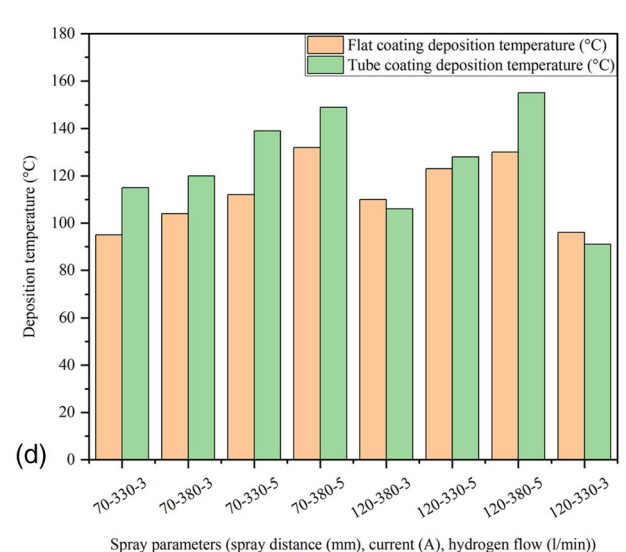




**Fig. 6** Comparison of coating characteristics for yttria-stabilized zirconia (8YSZ)-based thermal barrier coatings (TBCs) deposited on flat and tubular substrates using a coarser A&S powder under various spray parameters (spray distance, current, and hydrogen flow rate). Where (a) shows the porosity, while (b) illustrates deposition

condition was also achieved with a higher current and hydrogen flow (380 A and 5 slpm), while high-porosity coatings were produced under lower parameters (330 A and 3 slpm). These findings indicate that lower porosity is consistently achieved with increased current and hydrogen flow, regardless of spray distance, while lower settings result in higher porosity, suggesting that spray parameters such as current, spray distance, and hydrogen flow influence porosity similarly on both substrate types. Since both substrates show similar porosity, it implies that the particle melting, and impact conditions are not significantly affected by the change from a flat to a tubular surface under the tested parameters.



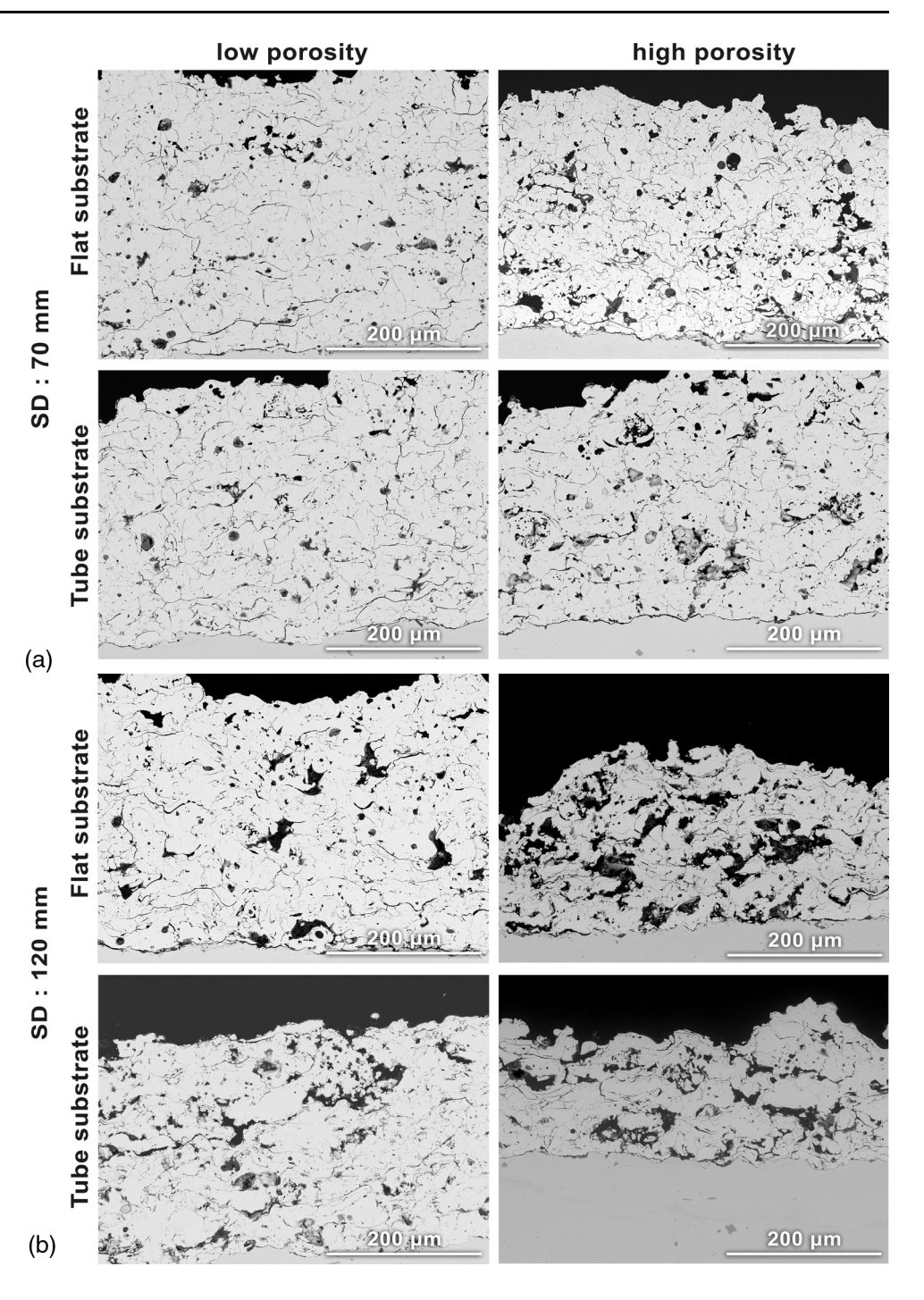


efficiency. (c) presents net plasma power (kW), and (d) displays the deposition temperature (°C) for coatings on both flat and tubular substrates. The error bars in (a) represent the standard deviation in porosity measurements

Deposition efficiency, as shown in Fig. 6(b), was also influenced by these parameters, with higher deposition efficiency observed at increased current and hydrogen flow settings. This trend aligns with the porosity results, as improved deposition efficiency often correlates with denser coatings. The net plasma power and deposition temperature in Fig. 6(c) and (d), respectively, provide further insights. Higher plasma power and deposition temperature correspond with lower porosity and higher deposition efficiency, particularly at increased current and hydrogen flow. This is likely because higher plasma power results in better particle melting, allowing for better splat spreading in the final coating.



Fig. 7 SEM images illustrating the microstructure of coatings produced with agglomerated and sintered (A&S) 8YSZ on flat and tubular substrates at varying spray distances and parameters. In (a), coatings are applied at a 70 mm spray distance. Low-porosity coatings on both flat and tubular substrates were achieved with spray parameters of 380 A and 5 slpm hydrogen flow, whereas high-porosity coatings on flat and tubular substrates were produced at 330 A and 3 slpm. In (b), coatings were applied at a 120 mm spray distance. Similarly, low-porosity coatings on flat and tubular substrates were generated at 380 A and 5 slpm, while high-porosity coatings on both substrates were obtained with 330 A current and 3 slpm hydrogen flow. The coatings in (b) appear thinner than in (a) because, at higher spray distances (120 mm), the number of spray passes was not adjusted to same coating thickness, resulting in thinner coatings compared to those sprayed at 70 mm spray distance

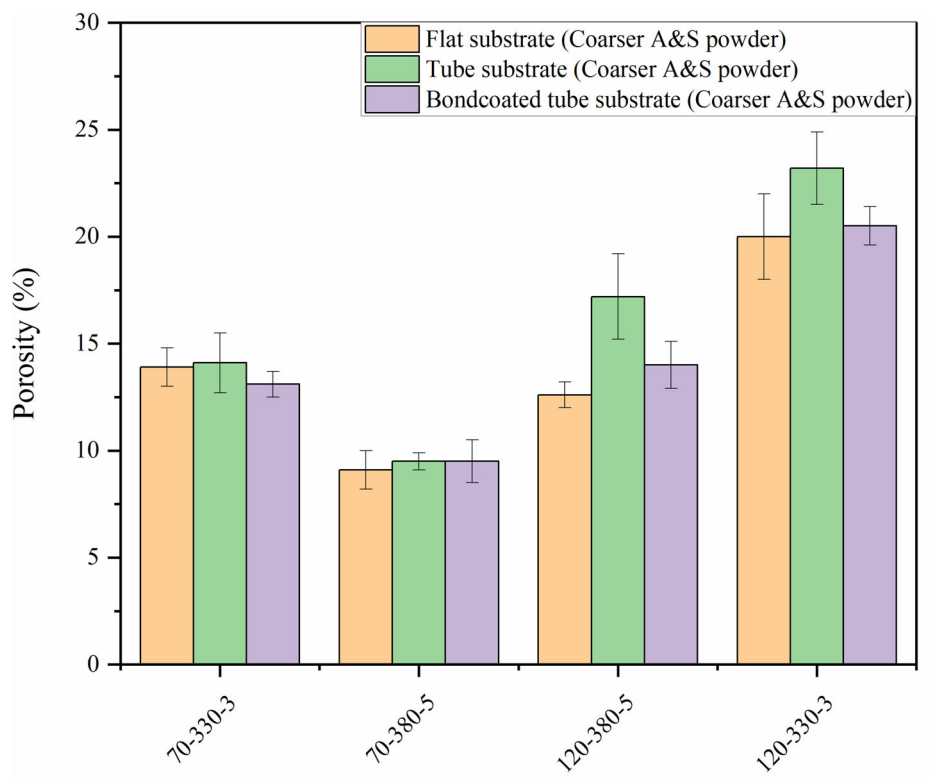


The SEM images in Fig. 7 corroborate these findings by illustrating the porosity levels in the microstructure of the coatings. The SEM images reveal that coatings produced under higher power settings (380 A and 5 slpm hydrogen flow) show denser microstructures with minimal voids on both flat and tubular substrates. In contrast, coatings produced under lower power settings (330 A and 3 slpm) exhibit higher porosity and less intersplat cohesion. The combined analysis of quantitative data and SEM images confirms that spray parameters, particularly current and

hydrogen flow, significantly influence porosity, deposition efficiency, and overall coating quality on both flat and tubular substrates. Therefore, it can be inferred that the ID-APS torch is effectively depositing coatings on both substrate types with comparable porosity levels when process parameters are matched. Furthermore, the coatings in image (b) are thinner than those in image (a) because the same number of spray passes was used, and the deposition efficiency is naturally lower at a larger standoff distance (120 mm) than at a smaller one (70 mm).



Fig. 8 Comparison of porosity in coatings produced with coarser agglomerated and sintered (A&S) 8YSZ powder on different substrates. The figure illustrates porosity levels for coatings applied on flat, ID-tubular, and bond-coated ID-tubular substrates



Spray parameters (spray distance (mm), current (A), hydrogen flow (l/min))

Figure 8 illustrates the porosity levels in coatings produced with coarser agglomerated and sintered (A&S) 8YSZ powder on various substrates, including flat, tubular, and bond-coated tubular substrates. Notably, when these coatings are deposited on bond-coated tubular substrates, the results indicate that porosity values remain within a similar range across all substrate types, with overlapping standard deviations. This overlap implies that the coatings applied using the F100 CONNEX ID torch exhibit consistent porosity characteristics regardless of substrate curvature, suggesting that the transition from flat to curved surfaces does not significantly alter the coating's microstructure or cumulative porosity. While Fig. 9 presents SEM cross-sectional images of the as-sprayed thermal barrier coating (TBC) system, which includes a CoNiCrAlY bond coat and an 8YSZ topcoat, applied to the inner diameter (ID) surfaces of tubular substrates using HVOF-ID and APS-ID torches, respectively. The images highlight the microstructural variations in porosity at two different spray distances of 70 mm and 120 mm. Specifically, Fig. 9(a) and (b) presents the coatings with the lowest and highest porosity at 70 mm, while Fig. 9(c) and (d) displays the lowest and highest porosity at 120 mm. When coatings are sprayed at 70 mm spray distance, coatings exhibit a denser microstructure, as can be seen in Fig. 9(a) and (b), where the porosity remains relatively low. In contrast, at the longer spray distance of 120 mm, as shown in Fig. 9(c) and (d), the porosity increases significantly, especially in Fig. 9(d), which the coating demonstrates highest porosity levels, approximately 20%, with an uneven topcoat thickness of  $160 \pm 27 \, \mu m$ .

# **Implications of ID Coating on the Deposition Process**

This section explores the effects of spray distance and other process parameters on the deposition characteristics of internal diameter (ID) coatings, focusing on microstructural, thermal, and stress implications.

## **Fracture Surface Analysis**

Fracture surface analysis of ID thermal barrier coatings (TBCs) reveals inherent defects, as listed in Fig. 10, that arise due to the nature of the thermal spray process. The intersplat (feature 2 in Fig. 10b) and intrasplat (features 3 and 7 in Fig. 10b and d) cracks arise from a combination of high thermal gradients, rapid quenching, and the intrinsic brittleness of fully and partially molten 8YSZ splats. Upon impact, the splats solidify within microseconds. Differential cooling between adjacent lamellae therefore generates tensile stresses both along splat interfaces and inside individual splats. These stresses are amplified when molten particle temperatures are low or nonuniform, conditions



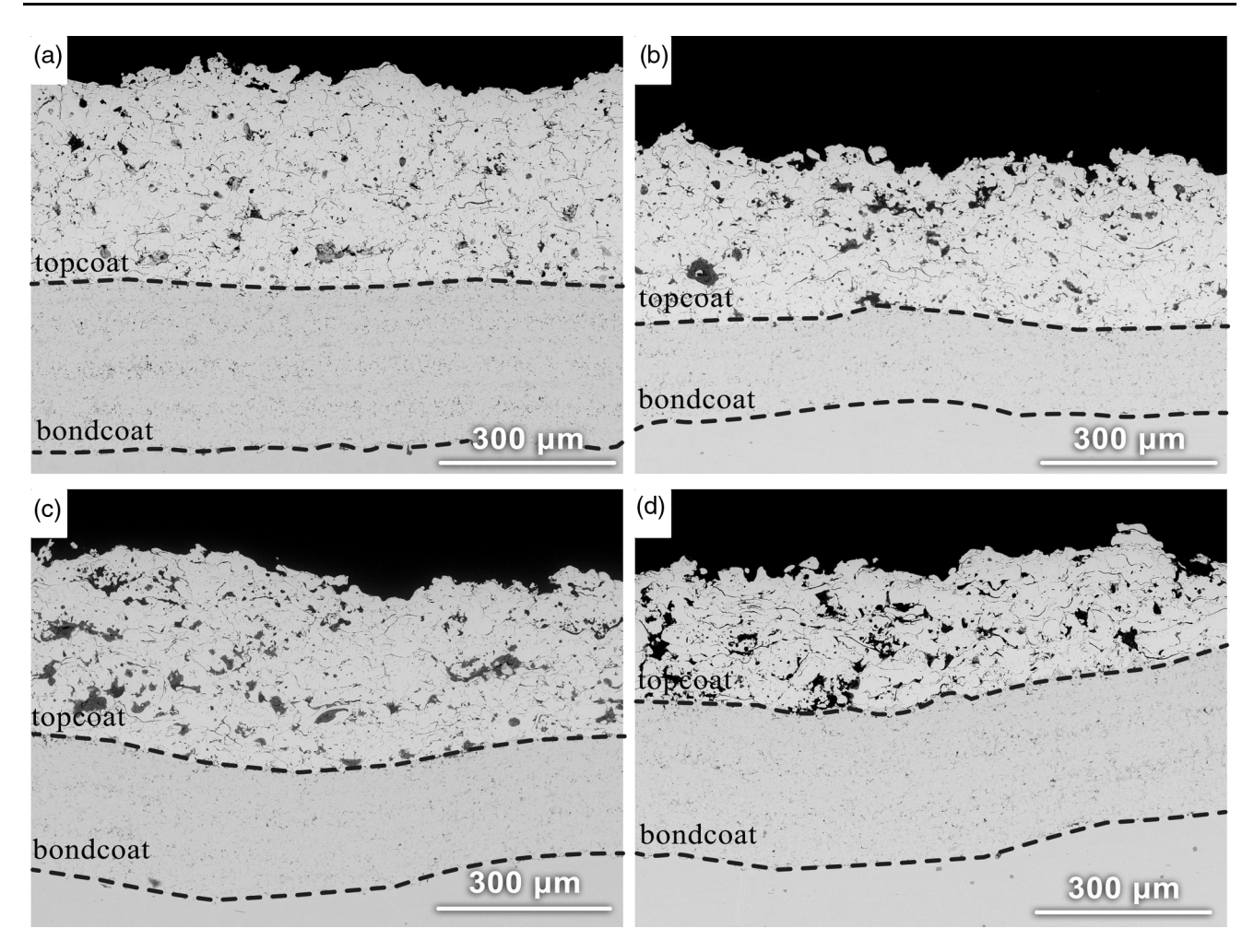


**Fig. 9** SEM cross-sectional images of the as-sprayed thermal barrier coating (TBC) system applied to the inner diameter (ID) surface of tubular substrates, consisting of a CoNiCrAlY bond coat and an 8YSZ topcoat deposited by HVOF-ID and APS-ID torches, respectively.

Images (a) and (b) show coatings with the lowest and highest porosity in the topcoat at a spray distance of 70 mm, respectively, while images (c) and (d) show the lowest and highest porosity in the topcoat at a spray distance of 120 mm, respectively

that occur more frequently at longer spray distances (120 mm, Fig. 10c and d) we also observe (i) gas-filled voids (feature 6) trapped inside splats and (ii) locally incomplete bonding (feature 7). Both act as stress concentrators and facilitate crack propagation. In contrast, splats deposited at 70 mm (Fig. 10a,b) retain more heat and flatten more uniformly. This yields better intersplat cohesion (feature 4). However, zones of incomplete splat contact (feature 1) remain visible even at short spray distance because the inherent nature of particle melting and impact precludes perfect interfacial wetting in APS coatings. These defects contribute to reduced thermal conductivity, allowing TBCs to function effectively as insulating barriers. For internal diameter (ID) TBCs, fracture surface analysis shows similar defect characteristics to those found in coatings applied with traditional plasma torches, consistent with existing (Ref 37, 38). However, ID plasma torches, which operate at limited spray distances, also have lower power output. This reduced power is especially problematic at larger spray distances, such as 120 mm, where defects like incomplete melting and increased porosity become more pronounced, directly affecting coating thickness due to reduced deposition rates (as shown in Fig. 6b). Particle diagnostics data from Fig. 11, based on 5000 particles, indicate that only around 24% of particles reach temperatures above 8YSZ's melting point (2800 °C) at a 120 mm spray distance, compared to 79% at 70 mm, leading to a higher presence of resolidified particles and increased porosity at greater spray distances. As low mechanical integrity of the coating can adversely impact the reliability of the TBC (Ref 29), it is crucial to understand the effects of power output, spray distance, particle temperature, and microstructural defects on the final coating quality. Correlating these factors suggests that ID TBCs are optimally produced at shorter, controlled spray distances. This approach balances the torch's low power with



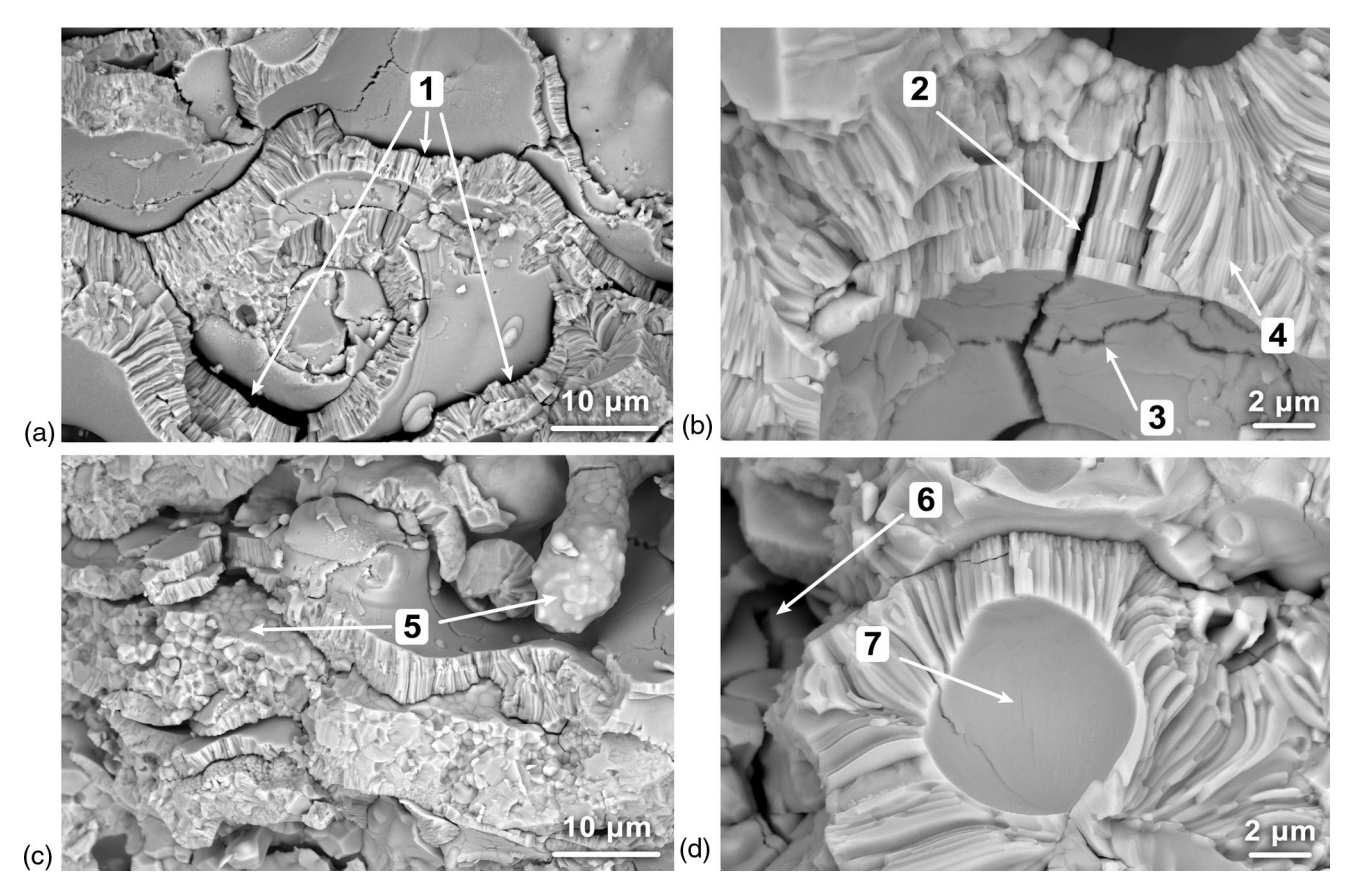


**Fig. 10** Backscattered electron (BSD) SEM images of fracture surface cross sections of plasma-sprayed agglomerated and sintered (A&S) 8YSZ coatings, applied using an internal diameter (ID) plasma torch, highlighting microstructural characteristics at different spray distances. Where (a) and (b) depict coatings sprayed at a 70 mm spray distance, while (c) and (d) show coatings sprayed at 120 mm spray

distance. Features marked in the images shows (1) regions with incomplete splat contact; (2) intersplat crack traversing multiple splats; (3) intrasplat crack within individual splat; (4) well-bonded splats with splat microcrack propagation across adjacent splats; (5) presence of resolidified particles; (6) void within a splat, suggesting gas entrapment; and (7) areas with incomplete bonding and voids

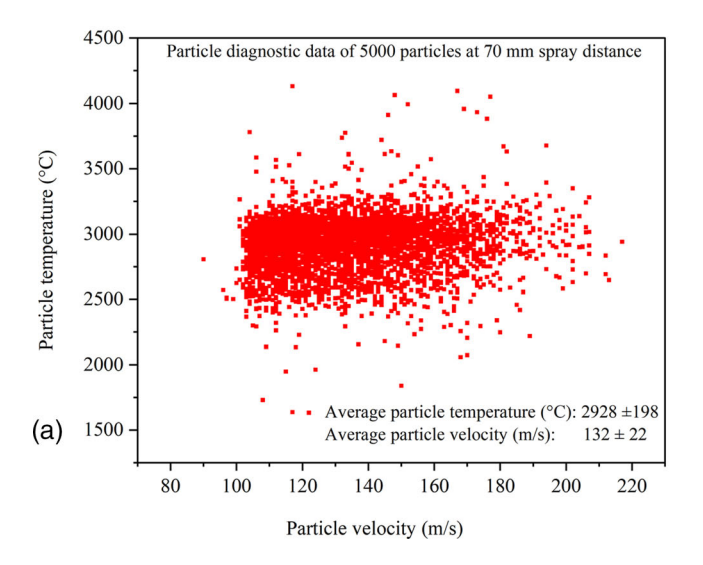
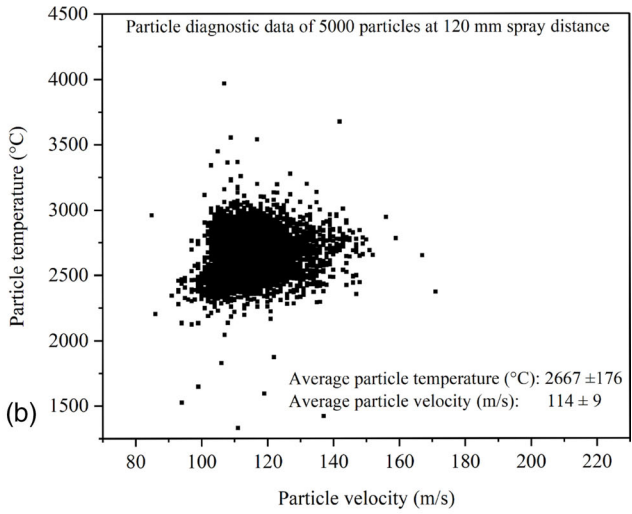


**Fig. 11** Particle diagnostic data of 5000 particles at two different spray distances, measured by the DPV-2000 system, showing the relationship between particle temperature (°C) and particle velocity (m/s). (a) Data at a spray distance of 70 mm, with an averaged



particle temperature of 2928  $\pm$  198 °C and an averaged particle velocity of 132  $\pm$  22 m/s. (b) Data at a spray distance of 120 mm, with an averaged particle temperature of 2667  $\pm$  176 °C and an averaged particle velocity of 114  $\pm$  9 m/s



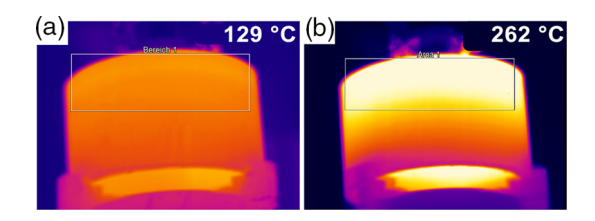


**Fig. 12** Thermographic analysis of substrate temperature during ID 8YSZ topcoat deposition using the ID-APS F100 CONNEX torch, showing (a) with cooling of 5.5 bar with compressed air and (b) without cooling

the need for a carefully regulated porosity, which enhances cohesion within the coating and improves its overall reliability.

# Thermographic Analysis of Substrate During Coating Deposition

The thermographic measurements aimed at observing the heat distribution over the substrate during coating deposition. Figure 12 illustrates the impact of the cooling system on both the deposition temperature of the coating and the average temperature measured over a defined rectangular region on the tubular substrate's outer surface. At a spray distance of 70 mm, with a current of 380 A and hydrogen flow rate of 5 slpm, the cooling system operating with compressed air at 5.5 bar significantly reduced temperatures during the coating process.

When the cooling system was off, the deposition temperature on the ID coating reached 325 °C, while the outer surface averaged temperature of the tubular substrate was recorded around 262 °C. With the cooling system activated, these averaged temperatures decreased to 163 °C and 129 °C, respectively. This corresponds to a temperature reduction of approximately 50% for the coating and for the substrate's outer surface. These results confirm that the integrated cooling system effectively manages heat buildup, so that there is no need for additional cooling devices using the F100 CONNEX ID torch under the investigated spray conditions.

### Residual Stress in as-Spayed Coatings

Given the thermomechanical nature of the deposition process in thermal barrier coatings, residual stresses are inherently retained within the coatings, which can significantly impact their lifetimes (Ref 39, 40). A detailed analysis of these residual stress measurements by ICP method provides valuable insights into the stress evolution and distribution within the coatings under various spray conditions. Understanding these factors allows us to identify optimal process parameters for developing reliable and durable ID coatings.

#### **Deposition Stress**

Deposition stress can be defined as the stress that arises from the rapid impact and solidification of particles during the coating process. This stress primarily a result of the sharp thermal gradients experienced by splats as they cool and solidify upon impact. At a spray distance of 70 mm, the deposition stress reaches a notably level of approximately 123.8 MPa for a coating thickness of 0.4 mm. Due to the shorter spray distance, particles retain significant thermal energy and velocity upon impact, resulting in a sharp thermal gradient as the splats cool quickly. This rapid cooling induces tensile stresses within the splats as they solidify, leading to the high deposition stresses observed (Ref 29). During this rapid cooling after solidification, several stress relaxation mechanisms occur, such as surface relaxation from edge effects, microcracking, and interfacial sliding from imperfect splat bonding. In contrast, at a longer spray distance of 120 mm, the deposition stress is significantly lower, recorded at 41.8 MPa. At this distance, particles have more time to dissipate heat before reaching the substrate, leading to a reduced thermal gradient upon impact. Thus, allowing stress relaxation mechanisms, such as microcracking and interfacial sliding, to relax quenching stress more effectively. As a result, tensile stress within the splats is minimized, resulting in a substantially lower deposition stress within the coating. This outcome aligns with the literature, which indicates that in ceramic coatings, extensive microcracking, and other relaxation mechanisms are critical in managing quenching stress (Ref 41).

#### Thermal Stress

Thermal stress, on the other hand, originates from the mismatch in thermal expansion between the coating and substrate, also varies with spray distance. At 70 mm spray distance, thermal stress for the coating layer of 0.31 mm thickness is measured at -9.3 MPa, indicating compressive stress resulting from rapid cooling and thermal contraction. In contrast, at 120 mm, thermal stress is only 1.9 MPa, indicating a more moderate thermal gradient and gradual cooling process.

## **Resultant Residual Stress**

The superposition of deposition and thermal stresses is the residual stress. For the 70 mm spray distance, the maximum residual stress in the coating layer reaches 114.4 MPa, while at 120 mm, it drops to 43.6 MPa. This decrease in residual stress at the longer spray distance indicates that a more moderate thermal gradient and deposition process lead to a stress state less prone to cracking and degradation. These findings suggest that



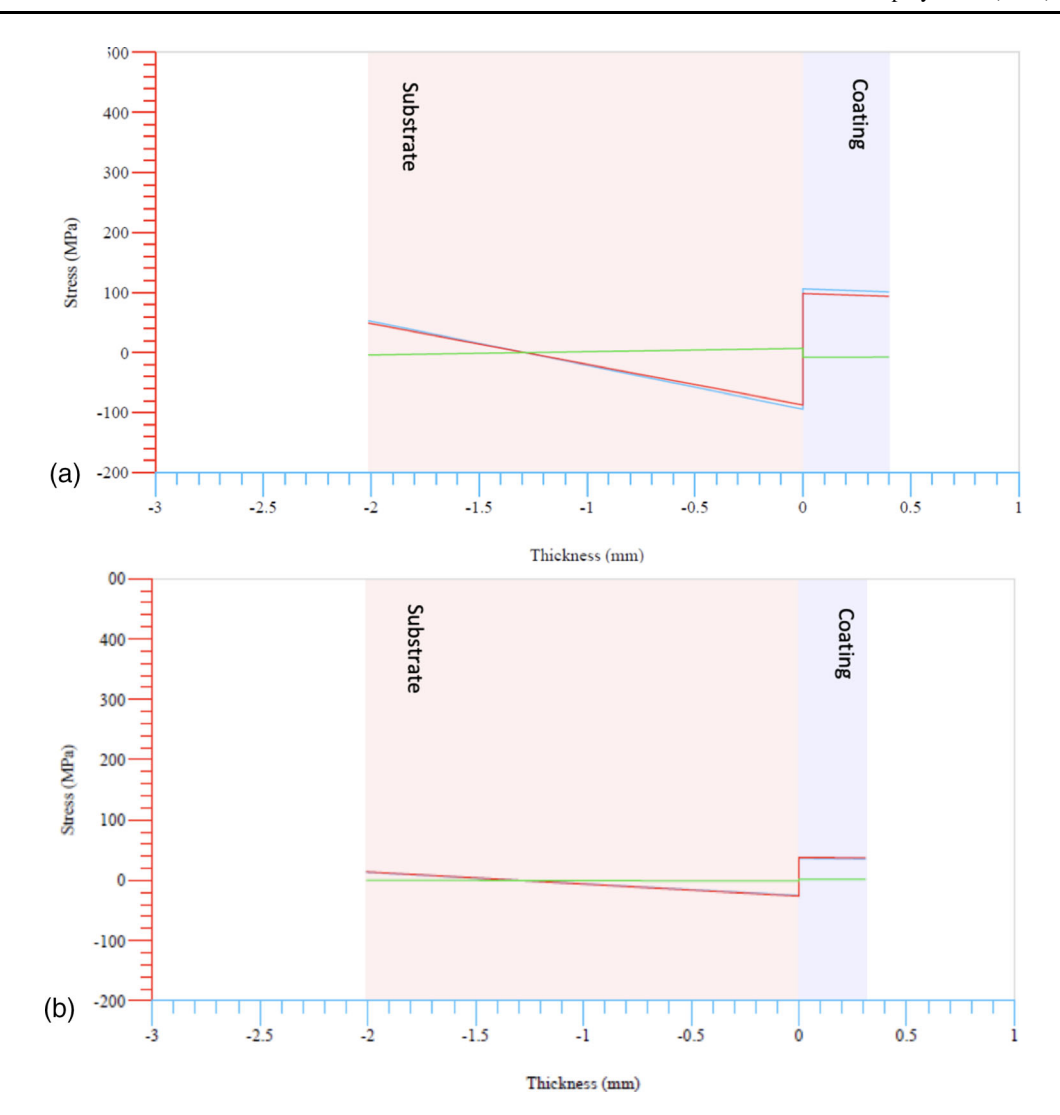


**Fig. 13** Residual stress profiles calculated based on in situ curvature measurements illustrating the stress distribution through the thickness of the substrate and coating, as measured by the ICP sensor. The blue line represents the deposition stress, the green line indicates the thermal stress, and the red line shows the resultant residual stress.

(a) shows measurements taken at a spray distance of 70 mm with 330 A current and 3 slpm hydrogen flow, while (b) shows measurements at a spray distance of 120 mm with 380 A current and 3 slpm hydrogen flow

longer spray distances allow for more stress relaxation within the coating, contributing to enhanced reliability and durability in high-temperature environments. Figure 13 illustrates the residual stress distribution through the substrate and coating thickness for the two spray distances obtained by ICP measurements.

#### Conclusion

This study examined several critical factors affecting internal diameter thermal barrier coatings (ID TBCs) by addressing key questions regarding powder characteristics, process parameters, substrate geometry, and implications on the spray process.

- 1. Influence of powder size and morphology: The analysis revealed that ceramic powder size and morphology significantly affect the microstructural properties of ID TBCs. In particular, agglomerated and sintered (A&S) powders with coarser particle sizes produced coatings with the highest porosity while maintaining a reasonable deposition efficiency among the powders studied. This highlights the importance of selecting appropriate powder characteristics to achieve desired porosity levels and deposition rates in ID TBC applications.
- Effect of process parameters: The study showed that different process parameters significantly affect the coating properties such as porosity, deposition efficiency (DE), and plasma power. DOE regression



analysis provided insight into these effects, showing that porosity and DE respond differently to certain parameters. By evaluating standardized coefficient estimates, the analysis identified optimal process settings that balance high porosity with efficient deposition. This approach provides a strategic framework for adjusting process parameters to improve coating quality in ID TBC applications.

- 3. Comparison of the coatings on flat and curved substrates: The results indicate that ID coatings on tubular substrates have similar microstructural characteristics as coatings on flat substrates, especially in terms of porosity, emphasizing that substrate curvature does not fundamentally alter the microstructure.
- 4. Fracture surface analysis revealed structural inconsistencies in coatings applied at longer spray distances, which can undermine coating reliability. Residual stress measurements further demonstrated that different spray distances result in different stress profiles, highlighting the importance of optimizing the distance to provide coating integrity. Thermographic analysis confirmed the benefits of an integrated ID torch cooling system that effectively controls heat buildup. These results underscore the implications of spray distance on the deposition of ID TBCs.

The process window defined in this study will serve as the baseline for a future study examining splat morphology, adhesion strength, and the burner-rig/furnace cycling life of ID TBCs. Together, these two papers provide a unified framework linking spray parameters to the long-term durability of coatings on confined internal surfaces.

Acknowledgments This work is part of the ID TBC project, which was funded by the Deutsche Forschungsgemeinschaft (DFG, German Research Foundation)-project number 456827225. In addition, the authors would like to thank the project partners at the LWT institute, TU Dortmund, Germany: Prof. Dr. Wolfgang Tillmann, Dr. Ingor Baumann, MSc. Jonas F. Zajaczkowki for depositing the bond coats for the tubular substrates, with special thanks to Jonas F. Zajaczkowki for assisting in performing the thermographic measurement experiments. Furthermore, the authors would like to thank the following colleagues of the IMD-2, Forschungszentrum Jülich, Germany, for their support: Mr. Karl-Heinz Rauwald, Mr. Frank Kurze, for assisting during the plasma spray coating of the samples as well as Dr. Doris Sebold for their support with SEM images and Erhan Sucuoglu and workshop team for their support with preparing the tubular substrates.

Funding Open Access funding enabled and organized by Projekt DEAL.

**Open Access** This article is licensed under a Creative Commons Attribution 4.0 International License, which permits use, sharing, adaptation, distribution and reproduction in any medium or format, as long as you give appropriate credit to the original author(s) and the source,

provide a link to the Creative Commons licence, and indicate if changes were made. The images or other third party material in this article are included in the article's Creative Commons licence, unless indicated otherwise in a credit line to the material. If material is not included in the article's Creative Commons licence and your intended use is not permitted by statutory regulation or exceeds the permitted use, you will need to obtain permission directly from the copyright holder. To view a copy of this licence, visit <a href="http://creativecommons.org/licenses/by/4.0/">http://creativecommons.org/licenses/by/4.0/</a>.

#### References

- N.P. Padture, M. Gell, and E.H. Jordan, Thermal Barrier Coatings for Gas-Turbine Engine Applications, *Science* (1979), 2002, 296(5566), p 280-284.
- D. Stöver and C. Funke, Directions of the Development of Thermal Barrier Coatings in Energy Applications, J. Mater. Process. Technol., 1999, 92-93, p 195–202.
- 3. J. Smith, J. Scheibel, D. Classen, S. Paschke, S. Elbel, K. Fick, and D. Carlson, Thermal Barrier Coating Validation Testing for Industrial Gas Turbine Combustion Hardware, *J. Eng. Gas Turbines Power*, 2016 https://doi.org/10.1115/1.4031448
- R. Darolia, Thermal Barrier Coatings Technology: Critical Review, Progress Update, Remaining Challenges and Prospects, Int. Mater. Rev., 2013, 58(6), p 315-348.
- D.P.H. Hasselman, L.F. Johnson, L.D. Bentsen, R. Syed, H.L. Lee, and M.V. Swain, Thermal Diffusivity and Conductivity of Dense Polycrystalline ZrO<sub>2</sub> Ceramics: A Survey, Am. Ceram. Soc. Bull., 1987, 66(5), p 799-806.
- J. Gutleber and J. Tewes, "Neuartige HVOF-Technologie für das Beschichten kleiner Innendurchmesser [Novel HVOF Technology for Small ID Spraying)," Conference proceedings, (Erding), Gemeinschaft Thermisches Spritzen e.V. (GTS), Unterschleißheim, Deutschland, 2018, p 123-132.
- W. Tillmann, C. Schaak, L. Hagen, G. Mauer, and G. Matthäus, Internal Diameter Coating Processes for Bond Coat (HVOF) and Thermal Barrier Coating (APS) Systems, *J. Therm. Spray Tech*nol., 2019, 28(1–2), p 233-241.
- C.R.C. Lima and J.M. Guilemany, Adhesion Improvements of Thermal Barrier Coatings with HVOF Thermally Sprayed Bond Coats, Surf. Coat. Technol., 2007, 201(8), p 4694-4701.
- C. Wales, M. Tierney, M. Pavier, and P.EJ. Flewitt, Reducing Steam Transport Pipe Temperatures in Power Plants, *Energy*, 2019, 183, p 127-141.
- P.W.J. Marion, O. Drenik, C. Frappart, F. Kluger, M. Sell, A. Skea, and R. Vanstonee, "Advanced Ultrasupercritical Steam Power Plants", 1st IEA Clean Coal Centre Workshop on Advanced Ultra-Supercritical Coal-Fired Power Plants, Austria, Vienna, 2012.
- G.R. Holcomb, J. Tylczak, and R. Hu, Materials Performance in USC Steam Portland (No. NETL-PUB-195). National Energy Technology Lab. (NETL), Pittsburgh, PA, and Morgantown, WV (United States). In-house Research, 2011.
- X. Guo, W. Sun, A. Becker, A. Morris, M. Pavier, P. Flewitt, M. Tierney, and C. Wales, Thermal and Stress Analyses of a Novel Coated Steam Dual Pipe System for Use in Advanced Ultra-Supercritical Power Plant, *Int. J. Pressure Vessels Piping*, 2019, 176.



- M. Ekström, A. Thibblin, A. Tjernberg, C. Blomqvist, and S. Jonsson, Evaluation of Internal Thermal Barrier Coatings for Exhaust Manifolds, Surf. Coat. Technol., 2015, 272, p 198-212.
- 14. H. Kosaka, Y. Wakisaka, Y. Nomura, Y. Hotta, M. Koike, K. Nakakita, and A. Kawaguchi, Concept of "temperature swing heat insulation" in Combustion Chamber Walls, and Appropriate Thermo-Physical Properties for Heat Insulation Coat, SAE Int. J. Engines, 2013, 6(1), p 142-149.
- A. Babu, G. Koutsakis, S. Kokjohn, and M. Andrie, Experimental and analytical study of temperature swing piston coatings in a medium-duty diesel engine. SAE International *J. Adv. Curr. Pract. Mob.*, (2022-01-0442), 2022, p 235-248.
- J. Somhorst, W.U. De Goes, M. Oevermann, and M. Bovo, Experimental evaluation of novel thermal barrier coatings in a single cylinder light duty diesel engine (No. 2019-24-0062). SAE Technical Paper, 2019.
- G. Koutsakis, S. Miles, and J. Ghandhi, Assessment of in-cylinder thermal barrier coatings over a full vehicle drive cycle (No. 2021-01-0456). SAE Technical Paper, 2021.
- M. Andrie, S. Kokjohn, S. Paliwal, L. S. Kamo, A. Kamo, and D. Procknow, Low heat capacitance thermal barrier coatings for internal combustion engines (No. 2019-01-0228). SAE Technical Paper, 2019.
- A. Kawaguchi, H. Iguma, H. Yamashita, N. Takada et al., Thermo-Swing Wall Insulation Technology; - A Novel Heat Loss Reduction Approach on Engine Combustion Chamber (No. 2016-01-2333). SAE Technical Paper, 2016.
- N. Uchida, A Review of Thermal Barrier Coatings for Improvement in Thermal Efficiency of Both Gasoline and Diesel Reciprocating Engines, *Int. J. Engine Res.*, 2022, p 3-19.
- C.J. James, Analysis of Parasitic Losses in Heavy Duty Diesel Engines. Diss. Massachusetts Institute of Technology, 2012.
- R. Vaßen, M.O. Jarligo, T. Steinke, D.E. Mack, and D. Stöver, Overview on advanced thermal barrier coatings, *Surf. Coat. Technol.*, 2010, 205(4), p 938-942.
- S. Bose, Thermal barrier coatings (TBCs), In *High Temperature Coatings*; Elsevier: Amsterdam, 2007, p 155-232.
- M. Mutter, G. Mauer, R. Mücke, O. Guillon, and R. Vaßen, Systematic Investigation on the Influence of Spray Parameters on the Mechanical Properties of Atmospheric Plasma-Sprayed YSZ Coatings, J. Therm. Spray Technol., 2018, 27(4), p 566-580.
- A. Kulkarni, A. Vaidya, A. Goland, S. Sampath, and H. Herman, Processing Effects on Porosity-Property Correlations in Plasma Sprayed Yttria-Stabilized Zirconia Coatings, *Mater. Sci. Eng. A*, 2003, 359(1-2), p 100-111.
- G. Mauer, R. Vaßen and D. Stöver, Comparison and Applications of DPV-2000 and Accuraspray-G3 Diagnostic Systems, *J. Therm. Spray Technol.*, 2007. https://doi.org/10.1007/s11666-007-9047-2
- 27. J. Antony, *Design of Experiments for Engineers and Scientists*, 2nd ed. Elsevier, London, 2014.

- R. Vaßen, E. Bakan, and S. Schwartz-Lückge, Influence of Substrate Removal Method on the Properties of Free-Standing YSZ Coatings, Coatings, MDPI AG, 2021, 11(4).
- J. Matejicek and S. Sampath, In Situ Measurement of Residual Stresses and Elastic Moduli in Thermal Sprayed Coatings Part 1: Apparatus and Analysis, *Acta Mater.*, 2003, 51(3), p 863-872.
- I. Baumann, W. Tillmann, C. Schaak, K. Schmidt, L. Hagen, J. Zajaczkowski, G. Schmidtmann, G. Matthäus, and W. Luo, Internal Diameter Coating by Warm Spraying of fine WC-12Co Powders (-10 + 2 mm) with Very Short Spray Distances up to 10 mm, *J. Therm. Spray Technol.*, 2021, 30(5), p 1344-1364.
- 31. A. Nouri and A. Sola, Powder Morphology in Thermal Spraying, J. Adv. Manuf. Process., 2019, 1(3), e10020.
- 32. P. Fauchais, G. Montavon, and G. Bertrand, From Powders to Thermally Sprayed Coatings, *J. Therm. Spray Technol.*, 2010, **19**(1-2), p 56-80.
- A. T.J. Verbeek, "Plasma sprayed thermal barrier coatings: production, characterization and testing," Phd Thesis 1 (Research TU/e / Graduation TU/e), Mechanical Engineering, Technische Universiteit Eindhoven, 1992.
- 34. E. Pfender, Heat and Momentum Transfer to Particles in Thermal Plasma Flows, *Pure Appl. Chem.*, 1985, **57**(9), p 1179-1195.
- M.I. Boulos, P.L. Fauchais, and J.V.R. Heberlein, *Thermal Spray Fundamentals: From Powder to Part*, Springer, New York, 2021.
- M. Vardelle, A. Vardelle, and P. Fauchais, Spray Parameters and Particle Behavior Relationships During Plasma Spraying, *J. Therm. Spray Technol.*, 1993, 2(1), p 79-91.
- G. Mauer, R. Vaßen, and D. Stöver, Atmospheric Plasma Spraying of Yttria-Stabilized Zirconia Coatings with Specific Porosity, Surf. Coat. Technol., 2009, 204(1-2), p 172-179.
- J. Medřický, N. Curry, Z. Pala, M. Vilemova, T. Chraska, J. Johansson, and N. Markocsan, Optimization of High Porosity Thermal Barrier Coatings Generated with a Porosity Former, J. Therm. Spray Technol., 2015, 24(4), p 622-628.
- V. Teixeira, M. Andritschky, W. Fischer, H.P. Buchkremer, and D. Stöver, Effects of Deposition Temperature and Thermal Cycling on Residual Stress State in Zirconia-Based Thermal Barrier Coatings, Surf. Coat. Technol., 1999, 120-121, p 103-111.
- V. Lasseur, S. Goutier, V. MartinezGarcia, A. Denoirjean, E. Meillot, G. Mariaux, J. Absi, and A. Killinger, Residual Stress Evolution in Zirconia (Y8%) Coatings During Atmospheric Plasma Spraying for Substrates Under Rotating Kinematic, *J. Therm. Spray Technol.*, 2020, 29(6), p 1313-1321.
- S. Kuroda, T. Dendo, and S. Kitahara, Quenching Stress in Plasma Sprayed Coatings and Its Correlation with the Deposit Microstructure, *J. Therm. Spray Technol.*, 1995, 4(1), p 75-84.

**Publisher's Note** Springer Nature remains neutral with regard to jurisdictional claims in published maps and institutional affiliations.

